

UNIVERSITÀ DEGLI STUDI DI NAPOLI FEDERICO II



**Dottorato di Ricerca in Ingegneria Chimica
(XX ciclo)**

TESI DI DOTTORATO

***Particolato Nanometrico prodotto da
Motori a Combustione Interna***

Comitato scientifico

Candidato

RELATORI

Cinzia Tornatore

Prof. Antonio D'Alessio
DIC Università di Napoli "Federico II"
Prof. Andrea D'Anna
DIC Università di Napoli "Federico II"

CO – RELATORI

Dott.ssa Bianca Maria Vaglieco
Istituto Motori – CNR di Napoli
Dott.ssa Simona Silvia Merola
Istituto Motori – CNR di Napoli

*Not everything that can be counted counts,
and not everything that counts can be counted.*

Albert Einstein

INDEX

Introduction	5
Chapter 1:	8
PARTICULATE MATTER AND PARTICLES	8
1.1. Particulate matter and particles.....	8
1.2. Particulate and Particles from Internal Combustion Engines.....	10
1.2.1. Diesel engine	13
1.2.2. Spark Ignition engine	14
1.3. Carbonaceous particles formation	15
1.3.1. Gas phase.....	16
1.3.2. Solid phase	17
1.4. Particles Size.....	18
1.4.1. Equivalent Diameters	19
1.4.2. Fractal Aggregates.....	20
Chapter 2:	23
THEORETICAL BACKGROUND.....	23
2.1. Multiwavelength Extinction and Scattering Spectroscopy.....	23
2.1.1. Numerical procedure for the retrieving of Multiwavelength Extinction and Scattering data.....	25
2.2. Laser Induced Incandescence	29
Chapter 3:	34
EXPERIMENTAL APPARATUS.....	34
3.1. Introduction.....	34
3.2. Engines.....	37
3.2.1. Compression Ignition Engine.....	37
3.2.2. Spark Ignition Engine.....	39
3.3. Commercial Instruments.....	41
3.3.1. Gaseous emissions measurement	41
3.3.2. Particulate mass measurement	42
3.3.3. Particles measurement: Electrical Low Pressure Impactor (ELPI)	42
3.4. Optical experimental set up	45
3.4.1. BUVESS experimental apparatus	46
3.4.2. LII experimental apparatus.....	47

Chapter 4:	49
EXPERIMENTAL RESULTS: DIESEL ENGINE	49
4.1. Engine Operating Conditions	49
4.2. Exhaust Gas Recirculation.....	50
4.2.1. Effect on engine parameters, NO _x and Particulate emission.....	50
4.2.2. Effect on particles size distribution by ELPI measurements	53
4.2.3. Effect on primary particles size and chemical nature by LII and BUVESS measurements.....	55
4.3. Catalysed Diesel Particulate Filter.....	59
4.3.1. Loading phase.....	59
4.3.2. Regeneration Phase	61
Chapter 5:	65
EXPERIMENTAL RESULTS: SPARK IGNITION ENGINE	65
5.1. Engine Operating Conditions	65
5.2. Three way catalyst effect on engine emissions	66
5.3. Characterisation of the particles downstream of the TWC	72
5.3.1. Optical techniques (BUVESS and LII)	72
5.3.2. ELPI and SMPS measurements.	78
Conclusions	83
Bibliography	88

Introduction

Due to their potential adverse health effects, nanoparticles (smaller than 50 nm in diameter) emitted by vehicles have received increasing attention by the scientific community [1-4]. Several studies indicate that the toxicity of particles increases as their size decreases [5-7] and that inhaled nanometric carbon particles pass rapidly into the systemic circulation, causing pulmonary diseases [8]. For these reasons, as reported in the draft proposal for Euro 5/6 emissions standards, the upcoming normative will introduce number based Particulate Matter (PM) limits [9].

In recent years, a strong reduction of particulate mass concentration was obtained at the exhaust of diesel engines thanks to the new efficient injection systems and to the introduction of after treatment devices (diesel particulate filters). Nevertheless, the filters still enable a high number of ultrafine particles to pass in the engine exhaust [10]. Particles emissions from spark ignition (SI) engines are negligible if compared to diesel ones in terms of mass concentration; this is why the attention has traditionally been focused on the characterization and control of particulate from diesel vehicles. The gasoline vehicles have been exempted from PM standards through the Euro 4 standard. On the other hand, as reported in recent studies, under high load with rich mixture conditions, including cold starts and acceleration, SI engines emit high number concentration of particles in the sub-50 nm size range comparable to those from diesel engines [11-16]. Thus, Euro 5/6 regulations will introduce PM mass emission standards, numerically equal to those for diesels, for gasoline cars but only for those equipped with direct injection engines [9].

Although a sizing procedure is indicated in the draft Euro 5/6 legislation, at the present time the choice of a suitable method able to detect nanoparticles and to give information

about their mass, their number concentration and chemical properties appears very difficult.

Standard particle-collection methods require dilution systems and a sufficient period to obtain an adequate sample and an accurate measurement. Nevertheless, during the collection time, particles could change their composition [17]. Some particle collection instruments for determination of size distributions, are based on the motion of particles with respect to gases and are biased toward measuring the total mass of particles collected, not the number of particles [18]. The potential consequence of this is that a few large particles foreign to the internal combustion engine exhaust source may bias the results, obscuring the more important small-particle concentration.

Recent advances in diagnostic techniques make possible the characterization of particle in real time in engine exhaust using optical methods [19]. The optical techniques result a very powerful sizing methodology: they are real time, “in situ” and non-intrusive and they allow the characterization of primary particles in terms of size distribution and chemical nature.

In this thesis, optical techniques and commercially available instruments were used at the exhaust of a Common Rail diesel engine and of a Port Fuel Injection Spark Ignition engine in order to characterise the nanoparticles emissions in view of the upcoming new normatives. The engines used for the experiments were equipped with aftertreatment devices and they were representative of highest number of vehicles present on the Italian roads until the last year [20]. The nanoparticles at the engines exhausts were characterized in terms of number size distribution and chemical and physical properties. Two different optical techniques were used: Laser Induced Incandescence (LII) and Broadband Ultraviolet–Visible Extinction and Scattering Spectroscopy (BUVESS).

LII is a laser-based technique that is able to measure the mass and mean diameter of primary particles with a large measurement range, not limited by aggregate size and by complex retrieving procedure [21]. BUVESS is based on ultraviolet–visible multiwavelength extinction and scattering spectroscopy. It overcomes the intrinsic limitations of single wavelength techniques by using several spectral information to retrieve particle size distribution [22]. The analysis of BUVESS data gives information about particles chemical nature and their physical structure [23]. The optical results were compared with those obtained by Electrical Low Pressure Impactor (ELPI). It is a real-time measurement device, which enables to obtain number size distribution and mass concentration for particles in the size range 7 nm - 10 μm . All the measurements were completed by diagnostics of engine fundamental parameters and PM mass and gases concentrations measured by conventional instrumentations.

Chapter 1:

PARTICULATE MATTER AND PARTICLES

1.1. Particulate matter and particles

The term “particulate matter” (PM) is used to describe any substance, except pure water, that exists as a liquid or solid in the atmosphere under normal conditions and is of microscopic or sub-microscopic size but larger than molecular dimensions (about 2 Å) [24]. Among the atmospheric constituents, particulate matter is unique in its complexity since it is composed of solid and liquid particles of various nature and size. A full description of atmospheric particles requires specification of not only their concentration but also their size, chemical composition, phase and morphology.

U.S. EPA (Environmental Protection Agency) [25] reports the following classification of atmospheric particles:

- Ultrafine: Particles with an aerodynamic diameter lower than 0.1 μm
- Fine: Particles with an aerodynamic diameter in the range 0.1 – 2.5 μm
- Coarse: Particles with an aerodynamic diameter in the range 2.5 – 10 μm
- Supercoarse: Particles with an aerodynamic diameter higher than 10 μm

In addition to the above provided terminology, the EPA also categorizes particles as follows:

- Total Suspended Particulate Matter (TSP): Particles ranging in size from 0.1 micrometer to about 30 micrometer
- PM₁₀: particulate matter with an aerodynamic diameter less than or equal to 10 micrometers.

- PM_{2.5}: particulate matter with an aerodynamic diameter less than or equal to 2.5 micrometers.
- Nanoparticles: particles with diameters below 50 nm

Figure 1.1 displays a typical size distribution of atmospheric particulate matter that combines the two classification schemes discussed above.

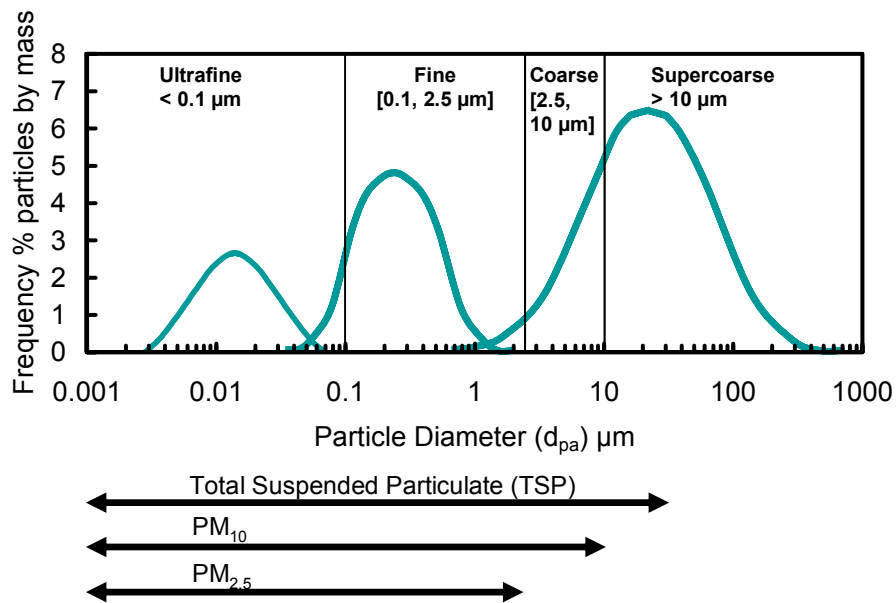


Figure 1.1. Typical size distribution of atmospheric particulate matter (U.S. EPA classification of particles four size categories)

Particulate matter in the atmosphere is of current interest because of its association with adverse health effects and its impact on the earth's radiation balance, visibility impairment and atmospheric chemistry.

Particles affect climate by changing the flow of radiant energy from the sun to the Earth's surfaces and within the atmosphere. They are able to do this both directly, by scattering and absorbing solar radiation, and indirectly, by changing cloud properties, rain, snow, and atmospheric mixing.

Moreover, evidence accumulated over the past decades suggests that increased levels of particulate air pollution in the urban area are associated with increased respiratory and cardiovascular mortality and morbidity as well as worsening of asthma [26]. Specifically ultrafine particles contribute to the PM health effects for several reasons. Compared with larger particles on a mass basis, ultrafine particles have a higher predicted pulmonary deposition, greater potential to induce pulmonary inflammation, larger surface area, and enhanced oxidant capacity. Ultrafine particles also have the potential to cross the epithelium and enter the systemic circulation [27].

There are both natural and human sources of atmospheric particles. The major natural cause is represented by dust, volcanoes, and forest fires. Sea spray is also a large source of particles though most of these fall back to the ocean close to where they were emitted.

The main human sources of particles are combustion processes, mainly the burning of fuels in internal combustion engines and power plants, and wind blown dust from construction sites and other land areas where the water or vegetation has been removed. Some of these particles are emitted directly to the atmosphere (primary emissions) and some are emitted as gases and form particles in the atmosphere (secondary emissions).

In this scenario, the mass fractional contributions of motor vehicles to ambient PM are estimated to be in the range from 20 to 76% and from 35 to 92% for PM_{2.5} and PM₁₀, respectively [28].

1.2. Particulate and Particles from Internal Combustion Engines

As source of ultrafine particles and nanoparticles in the urban environment, internal combustion engines have attracted large interest by the scientific community. In Figure

1.2 is reported the Italian situation in terms of contribution of different internal combustion engine vehicles on particulate emission.

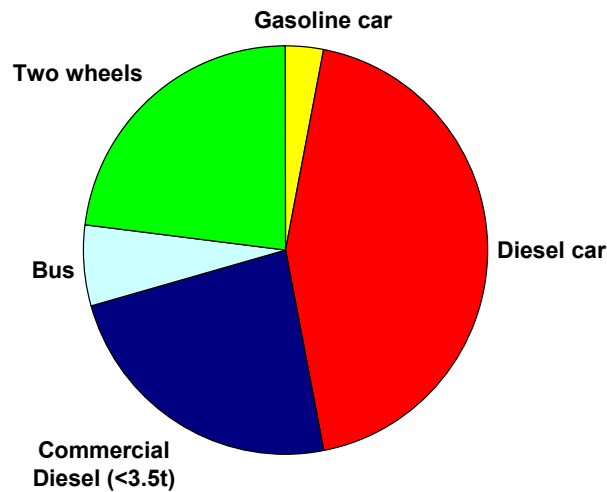


Figure 1.2. Typical distribution of particulate exhaust emission in Italian urban area evaluated for 2005 [29].

Both diesel and gasoline exhausts contribute to the emission of particulate in the urban area, nevertheless, the nowadays normative regards diesel engines as the main source of combustion aerosols emissions.

In the last 20 years the optimization of the diesel combustion process and the application of after-treatment devices reduced the particles mass concentration at diesel vehicles exhaust but it led to a significant reduction in particles size, thus high number concentration of nanoparticles is detectable [30-32].

Several experimental investigations demonstrated that also spark ignition engines emit high number concentration of particles in the sub-50nm size range [15, 16, 33]. The presence of nanoparticles was also observed at the exhaust of Port Fuel Injection Spark Ignition (PFI SI) engines [13, 34, 35] that are considered a sort of clean engine with respect to PM emission.

In July 2005 the European Commission published a draft proposal for Euro 5/6 emissions standards: Euro 5 standards will become effective from September 2009 for new type approvals, and from January 2011 for all models. Euro 6 standards will become effective from September 2014 for new types, and from September 2015 for all models.

The draft Euro 5/6 legislation adopts a new PM mass emission measurement method developed by the UN/ECE Particulate Measurement Programme (PMP). The PMP program had the objective to develop and select PM measurement methods for EU type approval testing and development of future emission standards for light- and heavy-duty vehicles. For particle number measurement the program recommended a method using a condensation particle counter (CPC), a selected size range (23 nm - 2.5 µm), and sample pre-conditioning at 300°C in an evaporation tube. The procedure has been designed to count solid particles only, and to eliminate volatile particles

The PM mass emission limit will be changed to 3 mg/km: this change accounts for different results using the existing and the new measurement method. The particles number emission limit at the Euro 5/6 stage will be $5 \cdot 10^{11} \text{ km}^{-1}$, in addition to the mass-based limits.

Gasoline vehicles have been exempted from PM standards through the Euro 4 stage. Euro 5/6 regulations will introduce PM mass emission standards, numerically equal to those for diesels, for gasoline cars but only with DI engines.

At the time of adoption of the Euro 5/6 regulation, its mass-based PM emission limits could only be met by closed particulate filters. Number-based PM limits would prevent the possibility that in the future open filters are developed that meet the PM mass limit but enable a high number of ultra fine particles to pass [36, 37].

1.2.1. Diesel engine

Diesel particulate matter, as defined by the EPA regulations and sampling procedures (the mass collected on a fibre filter from exhaust that has been diluted and cooled to 52°C or below [38]), is a complex aggregate of solid and liquid material. It is mainly composed by carbonaceous particles generated in the engine cylinder during the combustion. The primary carbon particles form larger agglomerates and they combine with other components of diesel exhaust, both organic and inorganic. Generally, the diesel PM is divided into three basic fractions:

- Solids - dry carbon particles, commonly known as soot,
- SOF - heavy hydrocarbons adsorbed and condensed on the carbon particles, called Soluble Organic Fraction,
- SO₄ - sulphate fraction, hydrated sulphuric acid.

The actual composition of diesel PM depends on the particular engine and its load and speed conditions. "Wet" particulates can contain up to 60% of the hydrocarbon fraction (SOF), while "dry" particulates are comprised mostly of dry carbon. The amount of sulphates is directly related to the sulphur contents of the fuel [39].

A small amount of inorganic ash is composed by metal compounds in the fuel (if metallic additives are present) and lubrication [1, 40].

Diesel particles are very fine. The primary carbon particles have a diameter of 10 – 80 nm, while the agglomerated particles diameter is in the 80 nm to 1 micron range. Thus, diesel particulate matter is almost totally inhalable and has a significant health impact on humans [41].

A significant amount of particulate matter (e.g. 90 % of the number and 30% of the mass) is formed during exhaust dilution from particle precursors that are in the vapour phase in the tailpipe (e.g., sulphuric acid, fuel and oil residues). The gas to particle conversion process involves homogeneous nucleation, adsorption and absorption and is highly nonlinear [42].

1.2.2. Spark Ignition engine

Historically, gasoline engines have been exempt from the requirement to meet the particulate emissions standard for diesel engines. The justification has been that the gasoline engines produced particulate emissions that were on the order of 1% of diesel engines ones [43]. This was certainly the case during the development of recent legislation on diesel particulate. Present studies indicate that current gasoline SI engines often emit an increased fraction of nanoparticles especially during transient operation [43]. The number concentration of particles emitted by gasoline Ported Fuel Injection (PFI) engines has also been shown to increase significantly under high load, transient and cold start conditions.

Unlike PM emissions from diesel engines, the Spark Ignition engines ones are very variable. With reference to PFI engines, a typical baseline concentration of engine out PM emissions is on the order of 10^5 particles/cm³, however a spike is occasionally observed [34]. These spikes are found to be composed mainly of volatile particles. Analyses of particulates from PFI engines reveal that the bulk of the mass is ash with the second largest fraction of unburned lubricating oil. Carbon emissions are found to be significant only at high speed and load with mixture enrichment. The large ash fraction of gasoline PM includes a large percentage of metal compounds with calcium

and sodium evident at low load without EGR, and copper and magnesium predominant for operation with EGR [44].

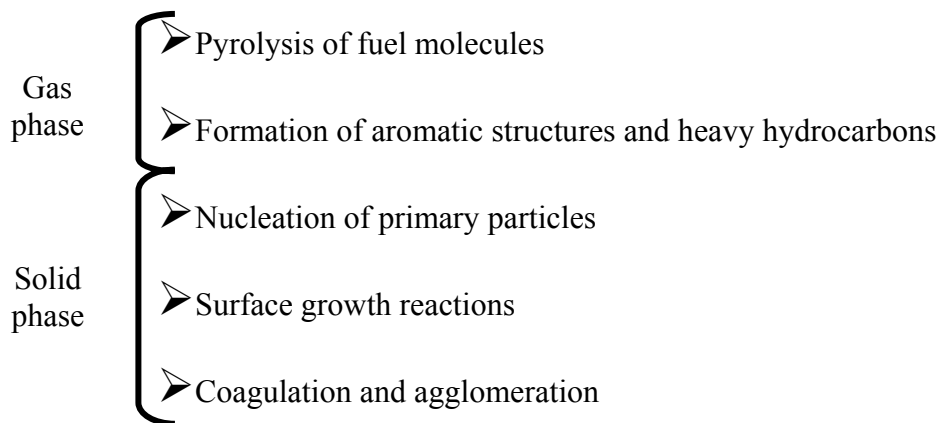
1.3. Carbonaceous particles formation

The soot formation is often observed during combustion of hydrocarbon fuels. Soot consists of carbonaceous particles and it can be identified in flames and fires as yellow luminescence.

Individual soot particles vary in shape from clusters to chains of spherules, where a soot cluster may contain as many as 4000 spherules. The spherules are called primary particles, their size varies in diameter from 10 to 80 nm, but mostly lies between 15 and 30 nm. The cluster or chain-like soot aggregates are defined as secondary particles [45].

The hydrogen and carbon ratio in soot ranges between 1:8 to 1:10.

Soot formation is a complex process, which involves many chemical and physical steps, it can be outlined as follows:



The main steps of soot formation are reported in Figure 1.3.

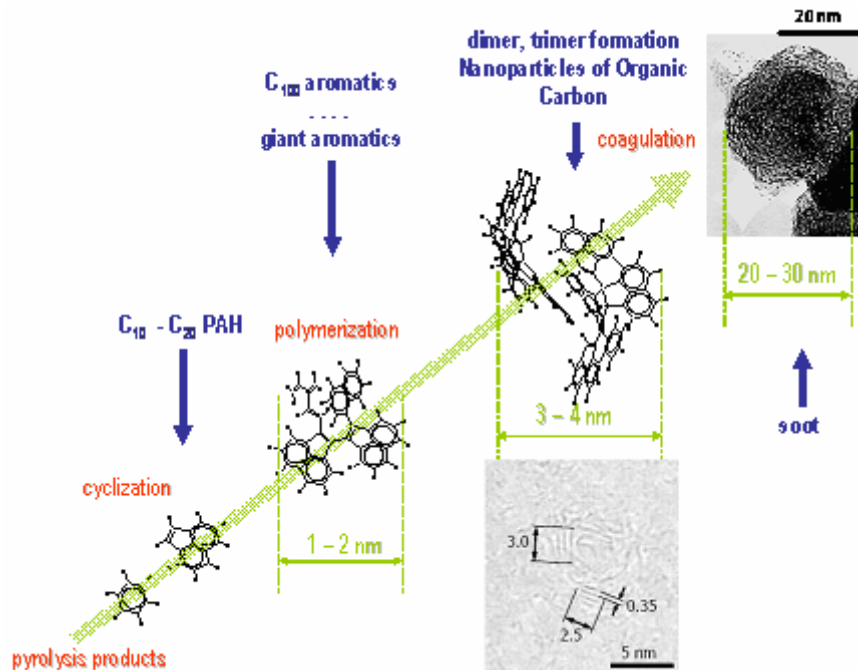


Figure 1.3. Formation of carbonaceous nanoparticles from combustion systems, adapted from [46].

A detailed kinetic model of soot formation usually contains two general parts, gas-phase chemistry, initiating the soot precursors, and solid-phase model [54].

1.3.1. Gas phase

The carbonaceous particles formation starts with fuel pyrolysis reactions and formation of the precursors. Starting, e. g., with an aliphatic fuel, the fuel molecules are first broken down into smaller hydrocarbon molecules and free radicals either by pyrolysis or oxidation reactions. Then the key step occurs, the formation of the first aromatic ring in the system, usually benzene or phenyl. This first ring appears as the nucleus for the formation of PAHs which are the most probable soot precursors as stated in recent studies [47-54]. Then the PAH growth takes place. The most popular mechanism of PAH growth is the HACA pathway developed by Frenklach and Wang [55, 56].

The model proposes a repetitive reaction sequence of two principal steps,

1. Abstraction of an H atom from the reacting hydrocarbon;
2. Addition of a gaseous C_2H_2 molecule to the radical formed.

A process parallel to the aromatics growth is their oxidation. Haynes and Wagner [45] and Neoh et al. [57] considered the hydroxyl radical as the primary oxidising agent.

1.3.2. Solid phase

The formation and evolution of soot particles includes processes like *soot particle inception*, *surface growth* and *oxidation*, *coagulation*, and *agglomeration* which are briefly described in the following:

The *soot particle inception* is a homogeneous process occurring in the gas phase environment. According to different investigations, it takes place at molecular masses between 500 a.m.u. [58], 300-700 a.m.u. [59], 1600 a.m.u. [60] and 2000 a.m.u. [61]. Above this values the PAH can be interpreted as solid particles rather than molecules. These first soot particles are roughly spherical in shape and have a C/H ratio of about 2. Upon aging, they can *coalesce* into larger spherical particles, undergo *surface reactions*, *dehydrogenation*, *oxidation* and *coagulation*. The soot that is emitted from combustion devices typically has a C/H ratio of approximately 10 and consists of agglomerates of spherical particles with an underlying graphitic-like structure.

Soot particle growth. The greater part of soot (> 95 %) is formed by surface growth rather than soot inception [62]. It is assumed that particle growth is similar to the formation of PAH, and acetylene and PAH are accepted to be the two main potential agents responsible for soot surface growth. It is a heterogeneous process, where adsorption and desorption processes at the surface have to be considered.

Soot particle coagulation. The coagulation is usually expressed as a process of *sticking* of two particles, which are *glued* together by a common outer shell generated by deposition similarly to surface growth. Coagulation takes place only for relatively small particles, which are characterised by high rates of growth (up to a diameter of 10 nm in low pressure premixed systems).

Soot particle oxidation. The process of soot particle oxidation is parallel to the surface growth. In fact, oxidation is also a surface reaction, which in principal should be treated as catalytic combustion [62].

Soot agglomeration. Soot agglomeration takes place in the late phase of soot formation when, due to lack of surface growth, coagulation is no longer possible [62]. As a result, open structured aggregates characterised by a log-normal size distribution are formed [62].

1.4. Particles Size

A particle can be characterized by its geometric or physical diameter. If the particle is spherical the meaning of this parameter is obvious, otherwise it does not have a precise meaning.

As reported in literature [63], soot aggregates are non-spherical particles.

When particles are non-spherical, contain void spaces, or when their material density is not known, the concept of size requires definition by one or more parameters. It often is most convenient to discuss particle size in terms of equivalent diameters, defined as the diameter of a sphere, which with a given instrument would yield the same size measurement as the particle under consideration [64].

In this section a classification of the most commonly used equivalent diameters is reported.

1.4.1. Equivalent Diameters

Volume Equivalent Diameter (d_{ve}). The volume equivalent diameter, also known as envelope equivalent diameter (d_e), is defined as the diameter of a spherical particle of the same volume as the particle under consideration [65]. For an irregular particle d_{ve} is the diameter that the particle would have if it were melted to form a droplet while preserving any internal void spaces. d_{ve} is equal to the geometric diameter d_p for spherical particles [66].

Mass Equivalent Diameter (d_{me}). The mass equivalent diameter is similar in concept to d_{ve} but with the difference that d_{me} does not include internal voids. Therefore, for a particle with no internal voids $d_{me} = d_{ve}$. If the particle contains internal voids, $d_{ve} > d_{me}$.

Electrical Mobility Diameter (d_m). The electrical mobility diameter is the diameter of a sphere with the same migration velocity in a constant electric field as the particle of interest [67]. Instruments such as the DMA and the SMPS measure d_m . This measurement is obtained via a force balance between the electrical force of a constant electric field on the net charges on the particle and the drag force experienced by the particle. The electrical force on the particle is:

$$F_{elec} = n_e E \quad (1.1)$$

Here n is the number of charges on the particle, e is the elementary unit of charge, and E is the strength of the electric field.

Aerodynamic diameter (d_a). In air pollution control, it is necessary to use a particle size definition that directly relates to how the particle behaves in a fluid such as air. The term "aerodynamic diameter" has been developed by in order to provide a simple means of categorizing the sizes of particles having different shapes and densities with a single dimension. The aerodynamic diameter is the diameter of a spherical particle having a density of 1 g/cm^3 that has the same terminal settling velocity in the gas as the particle of interest. Terminal settling velocity is a measure of the aerodynamic properties of the particle, and the aerodynamic diameter depends on the flow regime. Instruments such as the ELPI measure d_a .

For irregular particles of standard density, $d_m > d_{ve} > d_a$. Highly irregular particle populations, such as soot, will show significant differences in the size distributions measured simultaneously by mobility and aerodynamic techniques. These are not real discrepancies; instead, they merely capture the different dependence of both equivalent diameters on the fundamental particle properties. This phenomenon has been observed in several investigations [68, 69].

1.4.2. Fractal Aggregates

There are two common types of "aggregate particles" described in the literature [70]. The first type is a compact aggregate, whose external envelope is not far from spherical shape. The second type is represented by aggregate particles for which the external envelope is highly non-spherical. They are often termed fractal and have been studied

extensively, both theoretically and experimentally. Combustion emissions such as soot are a large source of fractal particles in the environment. A typical Transmission Electronic Microscope (TEM) image of diesel particulate collected at the exhaust of Common Rail Diesel Engine is reported in Figure 1.4.

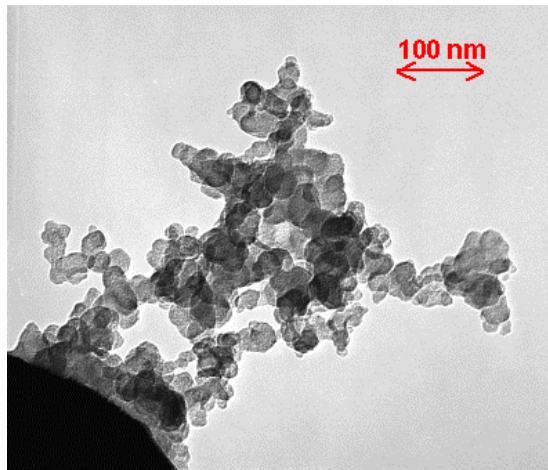


Figure 1.4. Typical TEM image of diesel particulate collected at the exhaust of Common Rail Diesel Engine

Fractal Dimension

Fractal dimension (D_f) is a parameter that is often used to describe aggregate particles.

The parameter, D_f , is defined from a relationship between the number of primary particles in an aggregate to a characteristic radius, R , typically the radius of gyration, by the following power law:

$$N_{pp} \approx R^{D_f} \quad (1.2)$$

Here N_{pp} is the number of primary particles in the aggregate. The fractal dimension can vary between 1 and 3. For spheres $D_f = 3$, compact agglomerates $D_f \approx 3$, and in the limit of infinitely long straight chain agglomerates $D_f \rightarrow 1$.

A range of intermediate values has been reported both for laboratory generated combustion aerosol and also for ambient aerosol [71]. The fractal dimension can be estimated via the mass mobility relationship [72] based on the scaling laws developed by Schmidt-Ott et al. [73]. In the mass-mobility relationship, it is assumed that the number of the primary particles is proportional to the particle mass m_p , which requires the primary particle size distribution to be constant for all values of N_{pp} as well as the assumption that the primary particle density is constant (which may not be strictly true if the aggregate is coated by a second species). The mass-mobility relationship is expressed as:

$$m_p = C' \left(\frac{d_m}{d_{pp}} \right)^{D_f} \quad (1.3)$$

Here C' is a constant and d_{pp} is the diameter of the spherules comprising the aggregate. Only the assumption of a constant primary particle size distribution is required to state that the particle volume is directly proportional to N_{pp} . Equation (1.3) can then be rewritten as

$$d_{ve}^3 = C'' \left(\frac{d_m}{d_{pp}} \right)^{D_f} \quad (1.4)$$

Since d_m can be measured and d_{ve} can be estimated as a function of N_{pp} (for a given d_{pp}), then Equation (1.4) can be used to estimate a fractal dimension based on the mass-mobility relationship with known values of d_{pp} and N_{pp} [64].

Chapter 2:

THEORETICAL BACKGROUND

2.1. Multiwavelength Extinction and Scattering Spectroscopy

The interaction of light radiation with matter can cause redirection of the radiation and/or transitions between the energy levels of the molecules. A transition from a lower level to a higher level with transfer of energy from the radiation field to the molecule is called absorption. Redirection of light due to its interaction with matter is called scattering, this phenomenon is strictly related to the heterogeneity of the sample. The extinction is the attenuation of an electromagnetic wave by scattering and absorption. Extinction and scattering spectroscopy can provide qualitative and quantitative information about the composition of a sample in terms of molecules and nanoparticles. The measured scattering signals obtained from a probe volume at a fixed scattering angle θ and at wavelength λ can be expressed, through a calibration procedure, in terms of the angular scattering coefficient $\beta_\lambda(\theta)$. This quantity is defined as the energy scattered at the angle θ from a unit volume, per unit solid angle, for an incident beam of unit intensity.

When the incident light comes from an unpolarised source, as in our case, scattering coefficient $\beta_{\text{unp},\lambda}(\theta)$ is:

$$\beta_{\text{unp},\lambda}(\theta) = N \cdot C_{\text{sca},\lambda}(\theta, D_p, n, k) \quad (\text{eq. 2.1})$$

Where $C_{\text{sca},\lambda}$ is the angular cross section for unpolarised scattering [74].

The extinction coefficient can be written as:

$$K_{ext}(\lambda) = N_i \cdot C_{i,ext}(\lambda) \quad (\text{eq. 2.2})$$

Where λ is wavelength of the incident beam, N_i and $C_{i,ext}$ are the number concentration and the extinction cross section of i^{th} compound, respectively. Whereas most of molecule extinction (or absorption) cross-sections in the ultraviolet-visible range are known by literature, the extinction cross-section of particle is a complex function of the chemical and physical properties. It can be interpreted in the framework of electromagnetic theory of light by:

$$K_{ext}(\lambda) = N \cdot C_{ext}(\lambda, D_p, n, k) \quad (\text{eq. 2.3})$$

Where N is the number density of the particle, D_p is the particle diameter and n and k are the real and the imaginary part of complex refractive index $m=n-ik$, respectively.

Assuming that the particles are spherical and constitute polydispersed system, scattering at fixed angle and extinction coefficients depend on particle diameter and they can be written according to Mie theory as:

$$\beta_{sca}(\lambda) = \int_{D_{min}}^{D_{max}} C_{sca}(m, \alpha) \cdot n(D_p) \cdot dD_p \quad (\text{eq. 2.4})$$

$$K_{ext}(\lambda) = \int_{D_{min}}^{D_{max}} C_{ext}(m, \alpha) \cdot n(D_p) \cdot dD_p \quad (\text{eq. 2.5})$$

Where

$$\alpha = \frac{\pi D_p}{\lambda}$$

α is the dimensionless size parameter and $n(D_p)$ is the number distribution.

It is possible to calculate the mass M , according to the relation:

$$M = \rho \int_{D_{min}}^{D_{max}} \frac{\pi D_p^2}{2} \cdot n(D_p) \cdot dD_p \quad (\text{eq. 2.6})$$

where ρ is particle-density.

The mean diameter D_m can be calculated as:

$$D_m = \frac{\int n(D_p) \cdot dD_p}{N} \quad (\text{eq. 2.7})$$

2.1.1. Numerical procedure for the retrieving of Multiwavelength Extinction and Scattering data.

In order to retrieve the multiwavelength extinction and scattering data, a numerical procedure was used; it allowed the evaluation of the number distribution of the particles and to characterize their chemical nature [75].

The procedure consisted in an iterative research of the particles size distribution and of their optical properties; it was based on the minimization of the difference between the experimental and the theoretical Lorenz-Mie scattering spectra. The same procedure is applicable also to the extinction spectra after the subtraction of the gas absorption

contributions. In Fig. 2.1 is reported a simplified block diagram illustrating the numerical procedure developed in LabView™ environment.

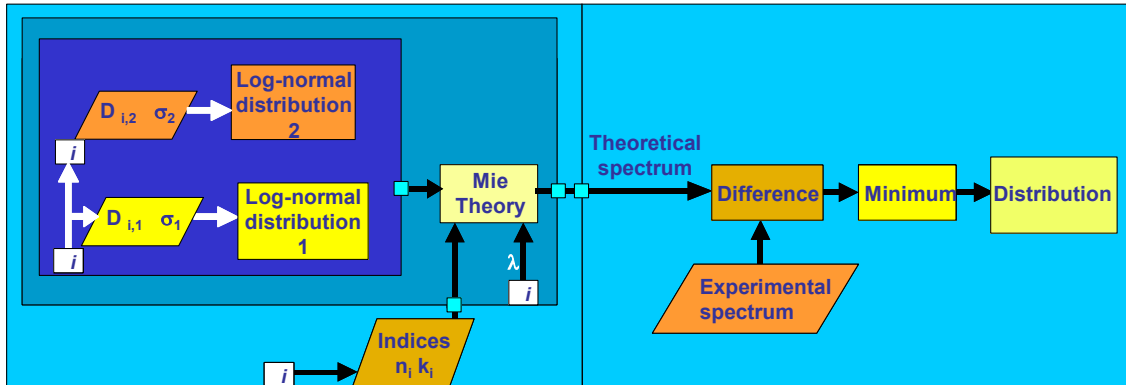


Figure 2.1. Block diagram of the procedure for retrieving the optical data.

In order to build up the scattering and extinction theoretical spectra, the refractive index was a necessary input for the procedure. An external database of optical properties accessible by the program was made up using literature data [1, 76]. For each refractive index given in input, the procedure selected the size distribution that minimised the difference between the theoretical and the experimental data. A log normal model was used for the particles size distributions in good agreement with the literature [77, 78], both unimodal and bimodal size distributions were considered. The central diameter of the log normal distribution was varied in a wide range (5 to 500 nm) in steps of 2 nm. Moreover different values for the distribution width were taken into account, in particular sigma was varied over a range of 0.1 – 0.3 in steps of 0.05.

At the end of the iterations, the size distribution and the optical properties corresponding to the lowest error achieved by the procedure were chosen as the final result.

With respect to carbonaceous matter, the database includes the refractive indices reported in Figure 2.2. They are listed according to the level of graphitization from the highest (a) to the lowest one (e).

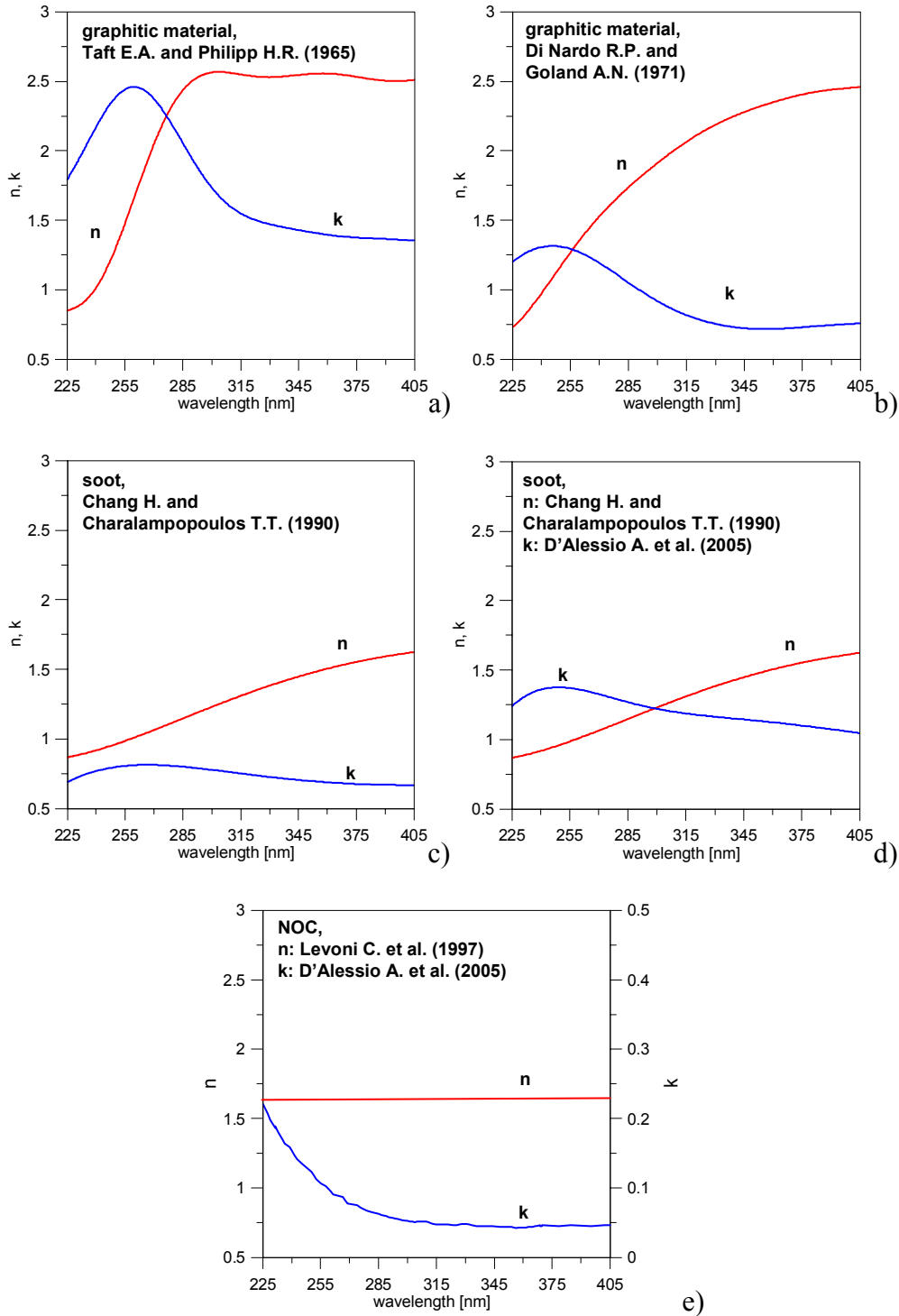


Figure 2.2. Selection of the optical properties reported in the database accessible by the numerical procedure for retrieving the optical data.

Taft and Phillip, have investigated the optical properties of carbon in a natural graphite crystal, a pyrolytic graphite sample and mechanically polished glassy carbon sheet [79]. The curve for natural graphite and pyrolytic graphite is nearly identical and it is shown in Figure 2.2a.

The refractive index reported in Figure 2.2b was obtained from the results reported by Di Nardo and Goland [80], they studied the optical properties of a 6 to 7 $\mu\text{g}/\text{cm}^2$ carbon foil prepared on potassium hydroxide as parting agent in the wavelength range 220 nm - 580 nm [81].

Chang and Charalampopoulos [82] determined the soot refractive index reported in Figure 2.2c by ex situ reflection coefficient measurements using compressed soot samples collected from flames.

D'Alessio et al. obtained carbon nanoparticles-optical properties in laminar premixed flat flames through the measurements of the UV-visible extinction coefficients and light scattering [83]. The imaginary part of soot and Nanoparticles of Organic Carbon (NOC) refractive indices are shown in Figure 2.2d and Figure 2.2e. The real part used for NOC index is reported in ref. [84].

In the retrieving of optical data, the simultaneous presence of different compounds in the same particle was considered. In particular, the optical property corresponding to a combination of various materials in “volume mixture configuration” could be the input of the numerical procedure [85]. In this case the refractive index m_{mixture} of the particle was computed by averaging the refractive index m_i of a single compound with respect to its volume fraction X_i according to the relation [86-88]:

$$m_{\text{mixture}} = \sum_i X_i \cdot m_i \quad (\text{eq. 2.8})$$

In the numerical procedure, different volume fractions X_i of the compounds in the particle were considered.

When the particles size distribution was obtained, the mass concentration was calculated by the equation (eq. 2.6) taking into account the densities associated to different materials according to the relation:

$$\rho_{mixture} = \sum_i X_i \cdot \rho_i \quad (\text{eq. 2.9})$$

2.2. Laser Induced Incandescence

The basic principle of laser induced incandescence measurements is to heat up the carbonaceous particles by a highly energetic laser pulse from ambient temperature and to analyse the enhanced thermal radiation [89, 90]. Carbonaceous particles absorb the laser light and emit a black body radiation that can be detected.

A time-dependent model for the particle energy loss can be developed, but it needs some hypothesis. First of all, the aggregates are idealized as composed by particles with the same diameter and touching at one point [91]. Although a soot particle is usually regarded as an agglomerate of primary spherical particles, a model for LII technique can be based on energy and mass balances for one spherical particle rather than for the whole aggregate. This viewpoint requires that all the particles in an aggregate have the same temperature; in addition, they have to be considered small enough to neglect internal temperature gradients. In this approach, individual monosized primary particles are considered.

The energy balance can be written as follows:

$$K_{abs} \pi \cdot a^2 q(t) = \Lambda(T - T_0) 4\pi \cdot a^2 + \frac{\Delta H_v}{W_s} \cdot \frac{dM}{dt} + q_{rad} + \frac{4\pi a^3}{3} \rho_s \cdot C_s \frac{dT}{dt} \quad (\text{eq. 2.10})$$

The various terms represent, respectively:

1. the absorption rate of laser energy where
 - K_{abs} is the absorption coefficient of soot
 - a is the particle radius
 - $q(t)$ is the temporal profile of the laser pulse;
2. the rate of heat transfer to the ambient by conduction where
 - Λ is the particle thermal conductivity toward the surrounding gases
 - T is the particle temperature
 - T_0 is the ambient gas temperature;
3. the energy expended in vaporization of soot carbon where
 - ΔH_v is the heat of vaporization of carbon
 - W_s is the molecular weight of carbon vapour species
 - $\frac{dM}{dt}$ is the rate of mass vaporization;
4. q_{rad} the rate of energy loss by black body radiation;
5. the rate of internal energy raise where
 - c_s is the specific heat of carbon
 - ρ_s is the soot density.

The mass conservation equation is:

$$\frac{dM}{dt} = 4\pi \cdot a^2 \rho_s \frac{da}{dt} = 4\pi \cdot a^2 \rho_s \cdot U_v \quad (\text{eq. 2.11})$$

where U_v indicates the thermal velocity [92].

(eq. 2.10) and (eq. 2.11) are a set of coupled differential equations numerically solvable in order to obtain particle's dimension $a(t)$ and temperature $T(t)$ time depending at specific exciting wavelength, ambient gas temperature T_o and particle's initial radius a_o .

Finally the LII signal must be calculated taking into consideration the density of primary particles, and the spectral bandwidth of detection, $\Delta\lambda$ around a central wavelength λ_0 (eq. 2.12).

$$LII(\lambda_0, t) = N_p 4\pi \cdot a^2(t) \cdot \frac{C_1 \varepsilon(t) \cdot \Delta\lambda}{\lambda_0^5 \cdot \left[\exp\left(\frac{C_2}{\lambda_0 T(t)}\right) - 1 \right]} \quad (\text{eq. 2.12})$$

Where C_1 and C_2 are the first and second Planck constant, N_p is the primary particles number density equal to the product between N (aggregates number density) and n_p (average number of nanoparticles per aggregate).

The LII signal at the maximum temperature, also called “prompt LII”, is proportional to:

$$\text{prompt LII} \propto N_p d_p^x$$

Where d_p is the particle diameter and the exponent x is:

$$x = 3 + \frac{154nm}{\lambda_0}$$

For λ_0 in the visible, this exponent is about 3 and the prompt LII signal is proportional to the soot volume fraction [91]. If values of particles number concentration are needed, an accurate calibration must be performed.

In order to obtain information on primary particles size, the temporal decay of the LII signal has to be evaluated. At some time after the laser excitation, the dominant cooling mechanism for the particle becomes conduction to the surrounding gas. So, the equation (eq. 2.10) becomes:

$$\frac{4}{3}\pi \cdot a^3 \rho_p c_p \frac{dT}{dt} = 4\pi \cdot a^2 \Lambda(T - T_0) \quad (\text{eq. 2.10a})$$

The difference between the particle surface temperature and the ambient gas, $\Delta T = (T - T_0)$, decays steadily in an exponential manner according to the equation:

$$\Delta T = A \cdot e^{-\tau^* \Delta t} \quad (\text{eq. 2.13})$$

where A is a constant. With determination of τ , the primary particle diameter may be inferred from the expression [93]:

$$d_p = \frac{12 \cdot k_g \cdot \alpha}{G \cdot \lambda_{MPF} \cdot c_p \cdot \rho_p \cdot \tau} \quad (\text{eq. 2.14})$$

where k_g is the thermal conductivity of the ambient gas, α is the accommodation coefficient, G is a geometry-dependent heat transfer coefficient, λ_{MPF} is the mean free path in the ambient gas, and c_p and ρ_p are the specific heat and density of the particle, respectively.

In this work a LII-based method for particle sizing concerned with the decay rate (cooling rate) of the LII signal was used. A typical ensemble decay curve detected by ICCD is shown in Figure 2.3.

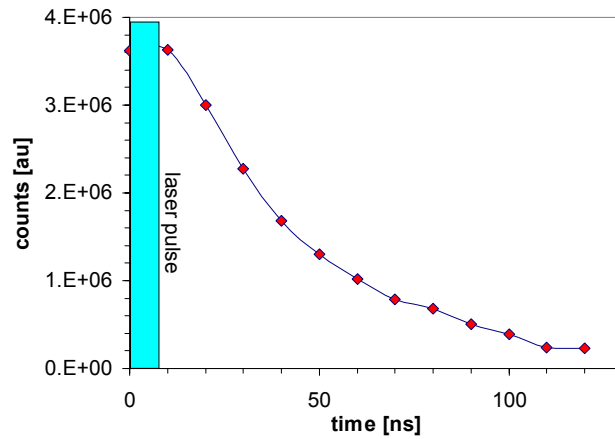


Figure 2.3. LII signal decay curve detected by the ICCD.

From the LII signal decay curve, the temperature decay was determined and it was fit to an equation of the form (eq. 2.13). The characteristic ΔT decay time, τ , was obtained and the primary particle diameter was calculated from the expression (eq. 2.14).

As reported in ref. [94], the primary particle size determined from the cooling rate is proportional to specific surface area available for conduction. Due to shielding and bridging of particles in an aggregate, the available specific surface area is substantially reduced, resulting in an apparent primary particle size that is significantly larger than the size one would measure with other techniques such as transmission electron microscopy (TEM) [95].

Chapter 3:

EXPERIMENTAL APPARATUS

3.1. Introduction

In this thesis, commercial instruments were used and non-conventional optical techniques were applied at the exhaust of a Common Rail diesel engine and of a Port Fuel Injection Spark Ignition engine in order to evaluate the effect of the operating conditions on the particles emission. The engines used for the experiments satisfied the European normative on emissions “Euro 3” and they were representative of highest number of vehicles moving on the Italian roads until the last year [96].

Table 3.1 reports a summary of the instruments and techniques at the exhaust of the IC engines. The regulated gaseous and solid emissions were measured by conventional systems.

In figure 3.1, the general sketch of the experimental setup is reported. An Electrical Low Pressure Impactor (ELPI) was employed to determine particles size distributions in the range 7 nm-10 μm . ELPI is an instrument based on electrical detection of inertially classified charged aerosol particles. Nowadays this kind of instrument is widely applied for automotive/engine exhaust measurements [97-100] since its rapid time response makes it an ideal tool for studying unstable concentrations and for the estimation of size distributions evolution. ELPI is a robust detector that can be applied to even rough environments, on the other hand for its functioning it must be coupled to a dilution system and this may induce strong modifications to chemical and physical structures of the particles. Moreover, ELPI has some limitation: in literature [101-103] a list of

nonideal behaviour of ELPI is presented, as particle bounce, wall or interstage loss, overloading or surface build-up, and losses due to electrostatic effects and to charger nonideal efficiency. In some experimental works [104], using a steady state speed, a continual decrease of small particles and a continual increase of bigger ones was observed: ELPI seemed to underestimate the apparent size of particles and, as a result, to overestimate their number.

In order to characterise the particles at the engines undiluted exhaust in terms of number size distribution and chemical nature, two optical techniques were applied. The first one was based on the Laser Induced Incandescence (LII). It was able to measure soot primary particles diameter. The second one was based on Broadband Ultraviolet-Visible Extinction and Scattering Spectroscopy (BUVESS); it took advantage of data at several wavelengths to retrieve primary particles size distributions. Moreover, BUVESS gave information about particles chemical nature. The optical techniques nowadays result a very skilful tool for the detection of particles. They are powerful “in situ” and non-intrusive techniques; on the other hand, they often need a retrieving procedure.

Until now, it is not recognised a univocal methodology for the measurements of particles size distribution and number concentration at the engines exhaust. Nowadays the European legislation on emissions indicates mass based limits for the particles but the standard methods of measuring exhaust particles (gravimetric measurements) have various shortcomings that can result in inaccurate data. Particles filter collection methods require complex and suitable dilution systems and a sufficient period of time to obtain an adequate sample and then an accurate measurement. Nevertheless, during the collection time, particles could change their composition.

In this thesis, the combination of different measuring methodologies with different sensitivities and operating principles was considered the best way for a wide range particles characterisation at the engines exhausts.

Gaseous and solid emissions	Devices for measurement	Measured quantity
NO _x O ₂	Electrochemical Sensors	Concentration
HC CO CO ₂	NDIR (No-Dispersive Infrared Detectors)	Concentration
Particulate	Opacimeter	Mass concentration
Particles <i>Commercial instrument</i>	ELPI (Electrical Low Pressure Impactor)	Aerodynamic diameter in the range 7 nm-10 μm
Particles <i>Optical techniques</i>	Extinction and Scattering UV-visible 190-600nm	Size distribution Chemical nature
	Laser Induced Incandescence	Mean Diameter Numeric Concentration

Table 3.1. Summary of the instruments and techniques and of the measured quantities.

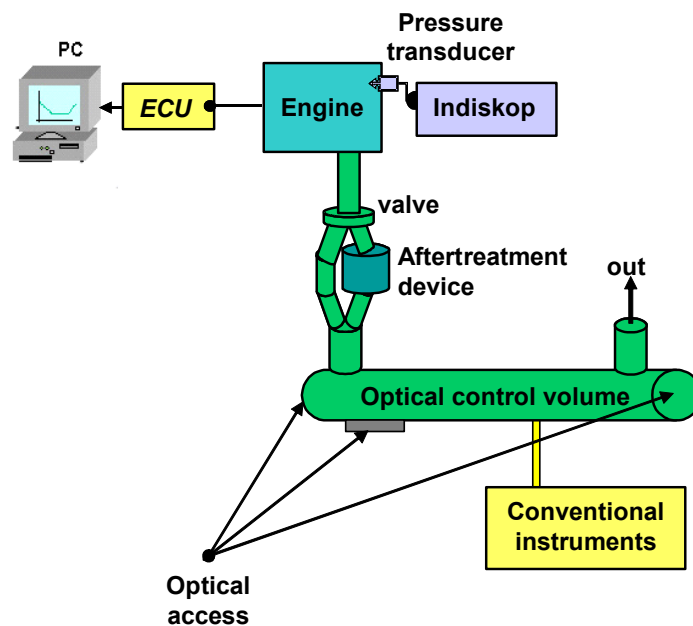


Figure 3.1. General sketch of the experimental setup

3.2. Engines

3.2.1. Compression Ignition Engine

A four-stroke Common Rail (CR) diesel engine, with four in-line cylinders 16 valves, a displacement of 1910 cc and a compression ratio of 17.5:1, was used. It was equipped with a CR injection system, which allows two injections (pilot and main) for each cycle (Unijet). The mean injection pressure reaches the maximum value of 1350 bar. The Engine Control Unit (ECU) has a PC interface that permits to control all engine parameters. More details about the engine are reported in Table 3.2.

The engine was provided with an Exhaust Gas Recirculation (EGR) cooled system. The basic element of the EGR circuit is an electro-valve mastered by the electronic control unit. The electro-valve receives an electrical signal (duty-cycle) and orders a pressure reduction to the mechanical valve (EGR valve) placed between the outlet and the inlet pipes. When the depression is applied, the EGR valve allows the addition of an exhaust gases fraction to the airflow. The whole process is controlled by the electronic control unit by means of characteristic diagrams saved in its memory. The effective EGR percentage can be obtained measuring the aspired air (\dot{m}) with and without EGR and using the following relation:

$$EGR\% = 1 - \frac{\dot{m}_{airwEGR}}{\dot{m}_{airw/oEGR}} \cdot \frac{p_{w/oEGR}}{p_{wEGR}} \cdot \frac{T_{wEGR}}{T_{w/oEGR}}$$

in order to get the exact EGR percentage values, corrections of pressure and temperature are necessary. The presence of exhaust gases in the inlet manifold does not imply the same reduction of the aspired fresh air. This is due to the contribution of exhaust gases thermal energy. It leads to an increase of the aspired fluid temperature and therefore to its expansion [105].

In this work, the expression “EGR%” in the experimental results indicates the duty-cycle value.

The engine exhaust was equipped with a 5.66” x 6” silicon carbide Catalysed DPF (known as CDPF, Catalysed Diesel Particulate Filter) coated with CeO₂ (400 g/ft³) and Pt (75 g/ft³). The catalyst coated directly the ceramic walls of the filter material to achieve spontaneous regeneration of collected PM at lower temperature with respect to non-Catalysed DPF. Typical regeneration temperatures were around 300-350 °C. The main features of the CDPF are summarized in Table 3.3.

Two specific sensors for temperature were installed upstream and downstream of the CDPF, and one for pressure drop was used to monitor the filter loading process. Specific investigations were performed on the engine test bed to verify the functionality of the CDPF.

All the measurements were carried out using standard diesel fuel whose properties are reported in Table 3.4.

Engine	1910 JTD
Engine Design	4 Cylinders, in-line
Bore/Stroke/Displacement	82 mm / 90.4 mm / 1910 cm ³
Max Torque	251 Nm / 2000 rpm
Max Power	77.2 kW / 4000 rpm
Compression Ratio	17.5 : 1
Max Speed	5000 rpm
Injection System	Common Rail Unijet™ (Bosch)
Max Injection Pressure	1350 bar

Table 3.2. Compression Ignition Engine specifications.

Material	Volume	Cell density	Wall thickness
Silicon carbide	4.0 dm ³	200 cpsi	0.36 mm

Table 3.3. Catalysed Particulate Filter specifications

Formula	C _n H _{1.8n}	
Cetane Number	51	
Density @ 15°C (kg/m ³)	834	
Distillation (°C)	150	2 %
	250	64 %
	350	85 %
Sulphur (ppm)	< 50	
Carbon (% wt)	86	
Hydrogen (% wt)	14	
Aromatics (%v)	25	

Table 3.4. Diesel fuel properties (standard diesel)

3.2.2. Spark Ignition Engine

A four-stroke 16 v – 1242 cc Port Fuel Injection (PFI) Spark Ignition engine, with four in-line cylinders, a compression ratio of 10.6:1 and a multipoint electronic injection system was used. More details about the engine are reported in Table 3.5. The engine was equipped with a three-way catalyst. Two lambda meters were used: the first one was located upstream of the catalyst in order to control the Air-Fuel ratio; the second one was placed downstream in order to check the catalyst operation. The exhaust temperature was monitored in real time by two thermocouples set along the pipe.

Engine type	Port Fuel Injection
Engine Design	4 Cylinders, in-line
Bore/Stroke/Displacement	70.8 mm / 78.9 mm / 1242 cm ³
Max Torque	114 Nm / 4000 rpm
Max Power	59 kW / 5000 rpm
Compression Ratio	10.6:1
Max Speed	6000 rpm

Table 3.5. Spark Ignition Engine specifications.

All the measurements were carried out using commercial gasoline fuel whose specifications are reported in Table 3.6.

Before starting the measurements, a warming procedure was carried out in order to avoid condensation and to activate the catalyst. Each engine operative condition was maintained for 10 minutes in order to guarantee the engine stability. For each test point the temperature of catalyst was higher than activation one (around 300°C).

For both engines, the in-cylinder pressure signals were measured for every cycle with a piezoelectric pressure transducer located in the engine head. A high precision Crank Angle Encoder was used for angle-based measurements. Flywheel generated trigger and crank angle degree marker pulses were produced at 0.05 crank angle degree (CAD) resolution. 150 cycles of pressure data were recorded on 0.1° crank angle resolved basis for each operating condition using a multi-channel analogical system. Integrated combustion parameters (e.g. heat release, IMEP) were calculated from the in-cylinder pressure data [106] using thermodynamics-based algorithms.

Aromatics (% v/v)	37.8
Benzene (% v/v)	0.94
Oxygen (% m/m)	2.7
Oxygenates: MTBE+ETBE (% v/v)	15
Density @ 15 °C (kg/m ³)	750
N° Octane (MON)	85.2
N° Octane (RON)	95.2
Acidity (mg KOH/g)	0.04
Stability (min.)	360
Lead (g/l)	0.005
Sulphur (mg/kg)	150

Table 3.6. Gasoline specifications.

3.3. Commercial Instruments

In order to carry out the characterization of the engines regulated emissions, commercial instruments were used. In particular NO_x, HC, CO CO₂ and particulate matter were measured.

3.3.1. Gaseous emissions measurement

The gaseous emissions were measured using fast analysers. The revealed species are: CO, CO₂ and HC by means of infrared analyser NDIR (No-Dispersive Infrared Detectors) and NO_x O₂ by means of electrochemical sensor.

3.3.2. Particulate mass measurement

The particulate mass concentration was evaluated by Opacimeter, it is a partial-flow system that measures the visible light attenuation (550 nm) from the exhaust gases, its probe was placed along the optical measurements pipe.

From the opacity N, mass concentration of particulate matter can be calculated according to the empirical equation:

$$c = k * \ln(100/(100-N))$$

with

$$c = \text{mass concentration [g/m}^3\text{]}$$

$$k = \text{calibration factor [g/m}^3\text{]}$$

$$N = \text{opacity [\%]}$$

By a comparison between opacity data and thermo-gravimetric results, a calibration factor $k = 0.2381$ was proposed [107].

3.3.3. Particles measurement: Electrical Low Pressure Impactor (ELPI)

ELPI is an electrical impactor working at low pressure; its sketch is reported in Figure 3.2. It is able to measure real time aerosol size distribution evaluating the aerodynamic diameter of particles in the range 7 nm-10 μm [100]. The exhaust sample first passes through a unipolar positive polarity charger where the particles are electrically charged by ions produced in a corona discharge. After the charger, the particles pass in a low-pressure impactor where they are classified according to their aerodynamic diameter. The stages of the impactor are electrically insulated and each stage is individually connected to an electrometer current amplifier. The charged particles collected in a

specific impactor stage produce an electrical current, which is recorded by the respective electrometer channel.

The current value of each channel is proportional to the number of particles collected, and thus to the particle concentration in the specific size range. The current values are converted to an aerodynamic size distribution using particle size dependent relations describing the properties of the charger and the impactor stages. The correspondence between each impactor stage and its cut diameter is reported in Table 3.7.

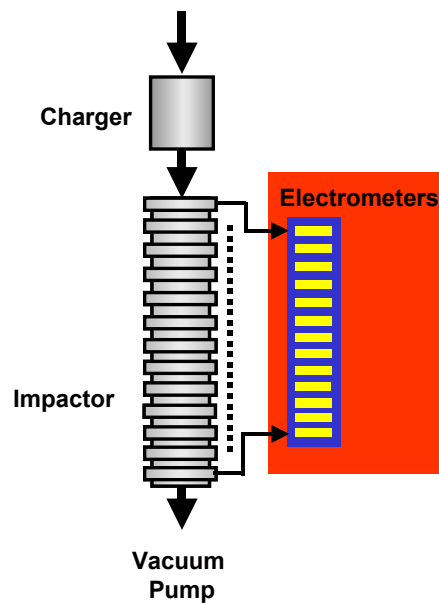


Figure 3.2. ELPI scheme.

Elpi Stage	1	2	3	4	5	6	7	8	9	10	11	12	13
Cut Diameter [nm]	7	28	54	91	154	261	381	611	946	1590	2380	3980	9890

Table 3.7. Correspondence between each impactor stage and the cut diameter of stored particles.

ELPI software provides values of mass concentration, mean diameter and volume of particles.

Particulate mass concentration can be directly obtained by ELPI software using the relation (3.1):

$$M_{ELPI} = \frac{\pi}{6} \cdot \rho \cdot \sum_{i=1}^{12} \frac{RD}{X_i(\rho)} \cdot d_i^3 \quad (3.1)$$

Where $X(\rho)$ is the current vector revealed by the system;

RD is the dilution ratio;

ρ is the mean mass density of the particles.

Particles mass concentration can also be evaluated utilizing the equation (3.2):

$$M_{ELPI} = \frac{\pi}{6} \cdot \rho \cdot (\bar{d})^3 \cdot \sum_{i=1}^{12} dN_i \quad (3.2)$$

Where \bar{d} is the particles mean diameter;

dN_i is the particles concentration on the i th stage;

ρ is the mean mass density of the particles.

Equation (3.2) gives more reliable results than equation (3.1). In fact, in the equation utilized by ELPI software, small contributions due to noise, oscillations or errors of correction on particles make the upper stages more relevant in the mass evaluation supplying imprecise values.

Equation (3.2) overcomes this problem calculating particles volume using the numeric density not affected by upper stages. However, sometimes the use of the formula (3.2) underestimates the real value of mass [108].

Before the ELPI a two steps dilution device named Fine Particle Sampler (FPS) is placed. FPS allows to sample and control dilution ratio and temperature of exhaust gas.

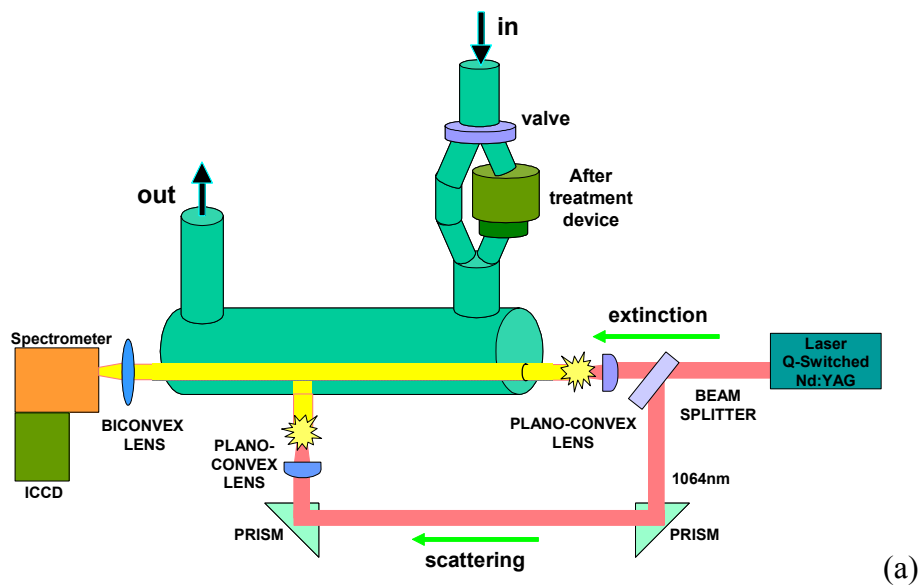
Primary dilution temperature is set around 250°C and the second one around 150°C.

3.4. Optical experimental set up

The schematic drawings of the optical experimental setup are shown in Figures 3.3 (a-b). For the diesel engine the section for the optical measurements was placed at 100 cm downstream the exhaust valves. For the spark ignition engine, a distance of 150 cm was chosen from the exhaust valves since the higher temperature of the exhaust gases could affect the optical devices operation. The above distances resulted as the best compromise to reduce the speed of the exhaust flow and to avoid coagulation effects caused by the increase of the permanence time in the test section.

Considering the low concentration of particles in the EURO 3 engines exhaust [9], an optical path length of 150 cm was chosen for both engines. The integration of the optical measurements over this path was sufficient to have a good signal to noise ratio.

The exhaust temperature was monitored in real time by two thermocouples set along the pipe, in order to evaluate possible condensation phenomena. A still plug valve permitted to the gas exhaust to flow and/or not in the optical measurement volume.



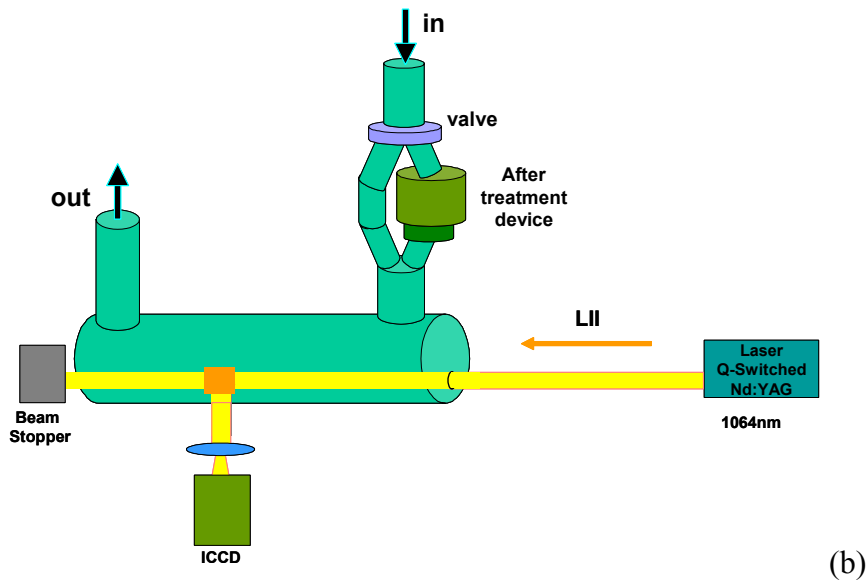


Figure 3.3. Optical set up for BUVESS (a) and for LII measurements (b).

3.4.1. BUVESS experimental apparatus

Broadband ultraviolet-visible extinction and scattering (BUVESS) measurements were carried out using a broadband pulsed light source. It was generated by the emission of a laser induced optical breakdown. [109] The breakdown spark was obtained focusing a Q-switched Nd:YAG laser beam, operating at the wavelength of $1.064 \mu\text{m}$, with max energy 390 mJ/pulse , 5 ns pulse duration and 8 mm beam diameter. The laser pulse was focused in air by Ultraviolet plane-convex lenses (10 cm focal-length) in order to avoid spurious sparks due to reflected light. The use of a beam splitter and two prisms allowed deviating the laser beam and performing the scattering measurements at 90° along an optical path of 15 cm .

BUVESS signals were collected and focused with an UV-grade fused silica biconvex lens (15 cm focal length) on the entrance slit ($200 \mu\text{m}$) of a spectrograph ($f/3$ with 15 cm focal length). It was equipped with a grating of 300 g/mm , blazed at 300 nm , with a dispersion of 19 nm/mm at 500 nm . The spectral image formed on the spectrograph exit

plane was detected with a gated intensified CCD (ICCD) camera (512 x 512 pixels) with every pixel of $19 \times 19 \mu\text{m}^2$. In this work, all the items were collected in order to obtain a single item with a high signal/noise ratio.

The measurements were performed in the spectral range UV-visible from 190 to 600 nm. A Mercury-vapour lamp was used to calibrate the wavelength of the spectrograph. The spectral efficiency of optical set-up was evaluated in the UV and visible region by a Deuterium lamp and Tungsten lamp, respectively. The absolute values of scattering coefficient were determined by measuring a flow of CO_2 at ambient pressure and temperature. CO_2 has a scattering cross section higher than air of about an order of magnitude [74] and is not flammable in presence of spark. The extinction coefficient measurements did not need any calibration.

In order to reduce the statistical uncertainty, the scattering and extinction measurements were carried out over 100 consecutive exhaust cycles, using laser shots at a frequency repetition of 20 Hz.

Synchronization between the engine, ICCD and light source was controlled by the unit delay with the signal coming from the angle shaft encoder.

3.4.2. LII experimental apparatus

The schematic drawing of the experimental apparatus for LII measurements is shown in Figure 3.2 b. The measurements were carried out exciting by the first harmonic of Q-switched Nd:YAG laser previously described, with 0.45 J/cm^2 laser fluence [110, 111]. This level of fluence was chosen in order to avoid photo-fragmentation phenomena. In the literature, radiative emissions from the C_2 Swan Bands [112] have been reported to interfere with the LII signal at high laser power densities especially with non uniform

beam profiles that provide high local fluence [113] (0.5 J/cm^2 at $1.064 \text{ }\mu\text{m}$). These interferences are one of the main problems that need to be addressed to make LII measurements. In this work the detection wavelength was fixed at 430 nm with a bandwidth of 10 nm FWHM in order to assure the absence of C_2 emission.

The LII signal was acquired at 90° angle to the direction of the incident beam using the gated intensified camera (ICCD); a 15 cm focal length lens was used.

In this experiment, the ICCD received an external timing signal from the Nd:YAG pump laser and it detected the LII signal just 10 ns after the laser pulse, delayed signal was detected because scattering interferences are generally short-lived relative to the LII signals. The ensemble decay curve was obtained by moving the gate via software.

The implementation of LII as a diagnostic technique required attention to excitation and detection conditions. The choice of excitation wavelength is mainly conditioned by avoiding the creation of photochemical interferences. High intensity ultraviolet laser pulses can produce undesirable emissions such as fluorescence from aromatic species and photofragment fluorescence. The near infrared wavelength of $1.064 \text{ }\mu\text{m}$, the fundamental of the Nd:YAG laser, has proven advantages in the generation of LII [114]. The binning of pixels on the x and y location was used to improve ICCD sensitivity. In this process, a number of pixels corresponding to the optical access were read out as a single pixel, this increased number of photons collected per binned pixel. Full Binning allowed using the ICCD chip as a Linear Image Sensor.

Chapter 4:

EXPERIMENTAL RESULTS: DIESEL ENGINE

4.1. Engine Operating Conditions

In this work, all the experiments were performed in steady state conditions at different engine speeds and loads (bmep). Each point was maintained for 10 minutes, allowing the stabilization of the engine operating conditions. The characterisation of the engine exhaust was performed in the conditions reported in Table 4.1.

The EGR percentages listed in the Table 4.1 are the optimised EGR values stored in the Common Rail ECU. They correspond to the best trade off between NO_x and particulate emitted by the engine.

rpm	bmep [bar]	EGR%	p rail [bar]	pilot vs TDC [°]	Q pilot [mm ³]	main vs TDC [°]	Q main [mm ³]
1000	2	56	335	-14.2	1.7	-6.5	6.8
1000	3	50	365	-14.3	2.0	-6.2	8.2
1500	2	46	480	-17.0	2.7	-6.2	7.0
1500	3	40	500	-17.0	2.9	-6.5	7.2
1500	5	0	570	-18.0	3.1	-5.7	11.5
1500	7	0	690	-21.7	3.9	-4.2	19.0
1500	9	0	760	-23.8	5.1	-3.3	23.0
2000	2	50	620	-19.5	3.6	-6.5	6.3
2000	5	0	710	-19.0	4.0	-5.8	11.9
3000	2	35	830	-25.4	2.4	-6.9	10.2
3000	5	0	915	-25.6	2.5	-7.2	14.9
3000	7	0	985	-26.1	2.7	-7.7	19.1
3000	9	0	1040	-27.7	2.8	-8.1	21.1
3000	12	0	1290	-30.9	3.1	-9.7	27.2

Table 4.1. Engine operating conditions

Then, in order to investigate the effect of the exhaust gas recirculation on the nanoparticles emission, the EGR percentage was varied in the range 0-60 for all the conditions listed in table 4.1 except for the highest speed. For these conditions the fuel injection strategies were maintained unchanged.

Finally, the effect of a catalysed diesel particulate filter (CDPF) on the nanoparticles emission was analysed. The filter loading phase and the regeneration were investigated.

4.2. Exhaust Gas Recirculation

The effect of EGR percentage on soot primary particles and aggregates was investigated at low engine speeds and loads.

The system of valves controlling the gas recirculation does not take advantage of whole duty-cycle dynamics, but only of a narrow range of values between 30% and 70% approximately. Thus, duty cycle from 0 to 30%, were not considered.

4.2.1. Effect on engine parameters, NO_x and Particulate emission

In Figure 4.1 the pressure signals detected in the combustion chamber at 1500 and 2000 rpm and BMEP=2bar are reported. When the EGR percentage increased, the maximum pressure signal of the cycle was reduced. In fact, the exhaust gases didn't take part in the combustion process and they only acted as thermal diluters. A temperature reduction was observed; therefore a decrease of thermodynamic performance and of the pressure peak was obtained [1].

Figure 4.2 reports the percentage deviation of the maximum pressure evaluated for each cycle with respect to the maximum value of averaged pressure calculated over 150

consecutive cycles at 1500 rpm – 2 bar for two EGR values (0 and 47%). Since the deviations were always lower than 3%, it's possible to state that the in-cylinder pressure signal was not influenced by cycle-to-cycle variation and the engine worked in high stability conditions.

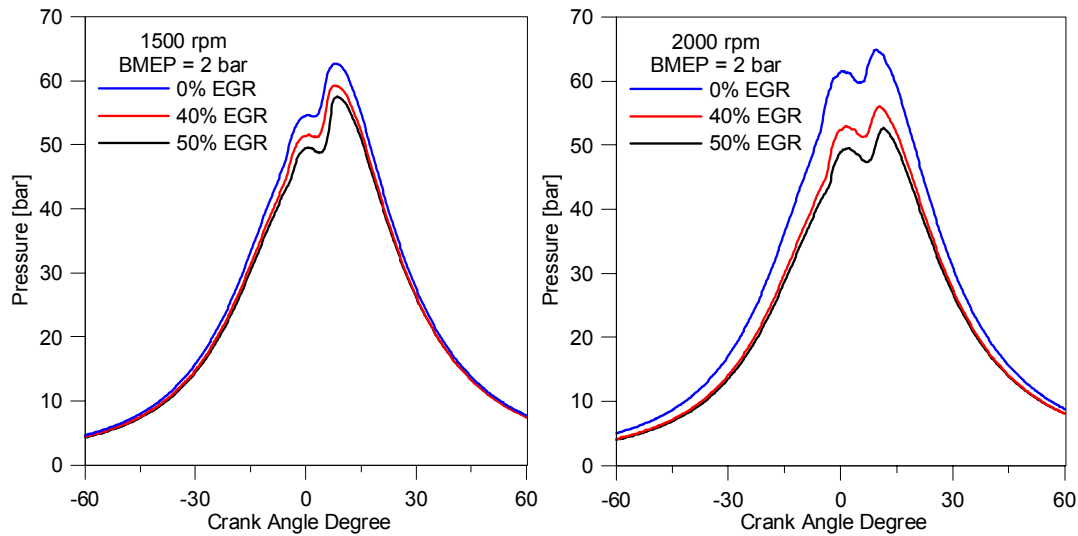


Figure 4.1. Pressure in the combustion chamber for different EGR% at 1500 and 2000 rpm and BMEP=2bar.

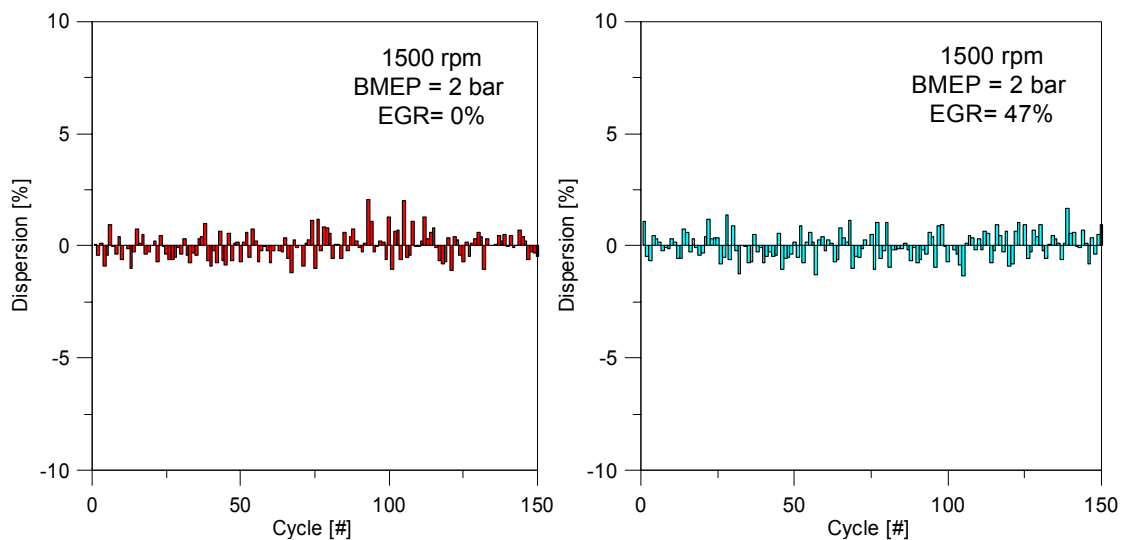


Figure 4.2. Percentage deviation of the maximum pressure evaluated for each cycle with respect to the maximum value of averaged pressure.

The indicated mean effective pressure (IMEP) was evaluated on an individual cycle basis and/or averaged on 150 consecutive cycles from the cylinder pressure data using conventional interpretation models [106]. Figure 4.3 reports the IMEP calculated on the whole power stroke and averaged on 150 consecutive cycles as function of EGR%. The percentage variation of IMEP was less than 3% for all the engine conditions. As a consequence the limits of driveability were maintained even with respect to the feeling of the driver.

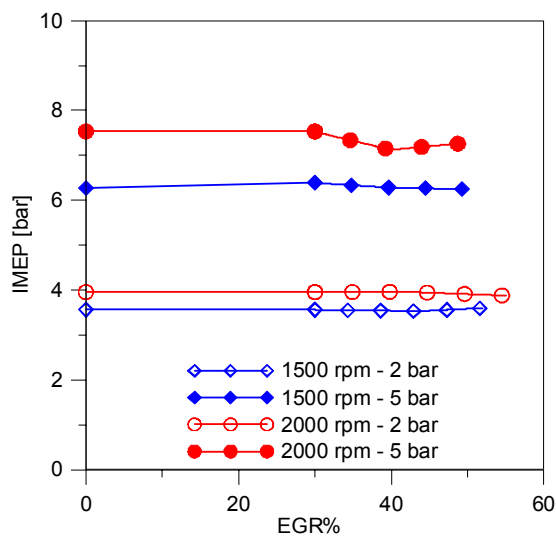


Figure 4.3. IMEP for different EGR% at 1500 rpm and BMEP=2bar.

The smooth evolution of IMEP was in contrast to the gas emission and Particulate Matter behaviours measured at the raw engine exhaust. In Figure 4.4 Nitrogen Oxides (NO_x) and PM concentrations for different EGR% values are reported. NO_x concentration suddenly decreased when EGR reached the value of duty cycle activation (30%). At the same value, an increase of particulate concentration was observed [107, 115] as expected due to the trade off NO_x-particulate [116-119]. Such effect was caused by the introduction in the combustion chamber of a gaseous mixture composed by air and exhausted gases. Due to the reduced availability of oxygen, the probability of a rich

combustion and soot particle formation increased. Even if diesel engines operate in air excess conditions, in the fuel side of the flame front it is always possible to find regions characterised by oxygen deficiency [120], this explains the occurrence of soot formation.

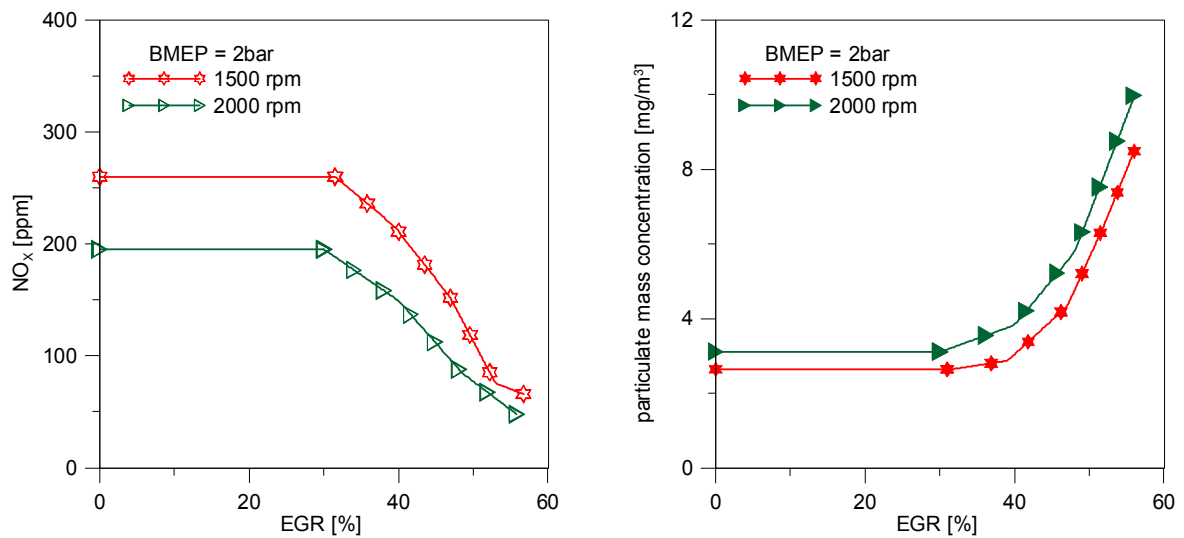


Figure 4.4. Nitrogen Oxides (NO_x) and Particulate Matter concentration for different EGR% for BMEP=2bar.

4.2.2. Effect on particles size distribution by ELPI measurements

In Figure 4.5 particles size distributions obtained by ELPI at 1500 and 2000 rpm are reported for different loads. Particles number concentration increased with the EGR: the peak concentration rose until one order of magnitude for the highest load and speed. For almost all the engine conditions, the size distributions showed a maximum at the third impactor stage, corresponding to a cut diameter equal to 54 nm. Moreover, the emission of a little fraction of particles larger than 300 nm at highest EGR, was the reason of the sharp raising of mass concentration that is a function of particle volume.

To analyse the effect of EGR on the different size classes of particles, the ratio between the number of particles collected on each ELPI stage and the total number of particles was calculated as it can be observed in Figure 4.6.

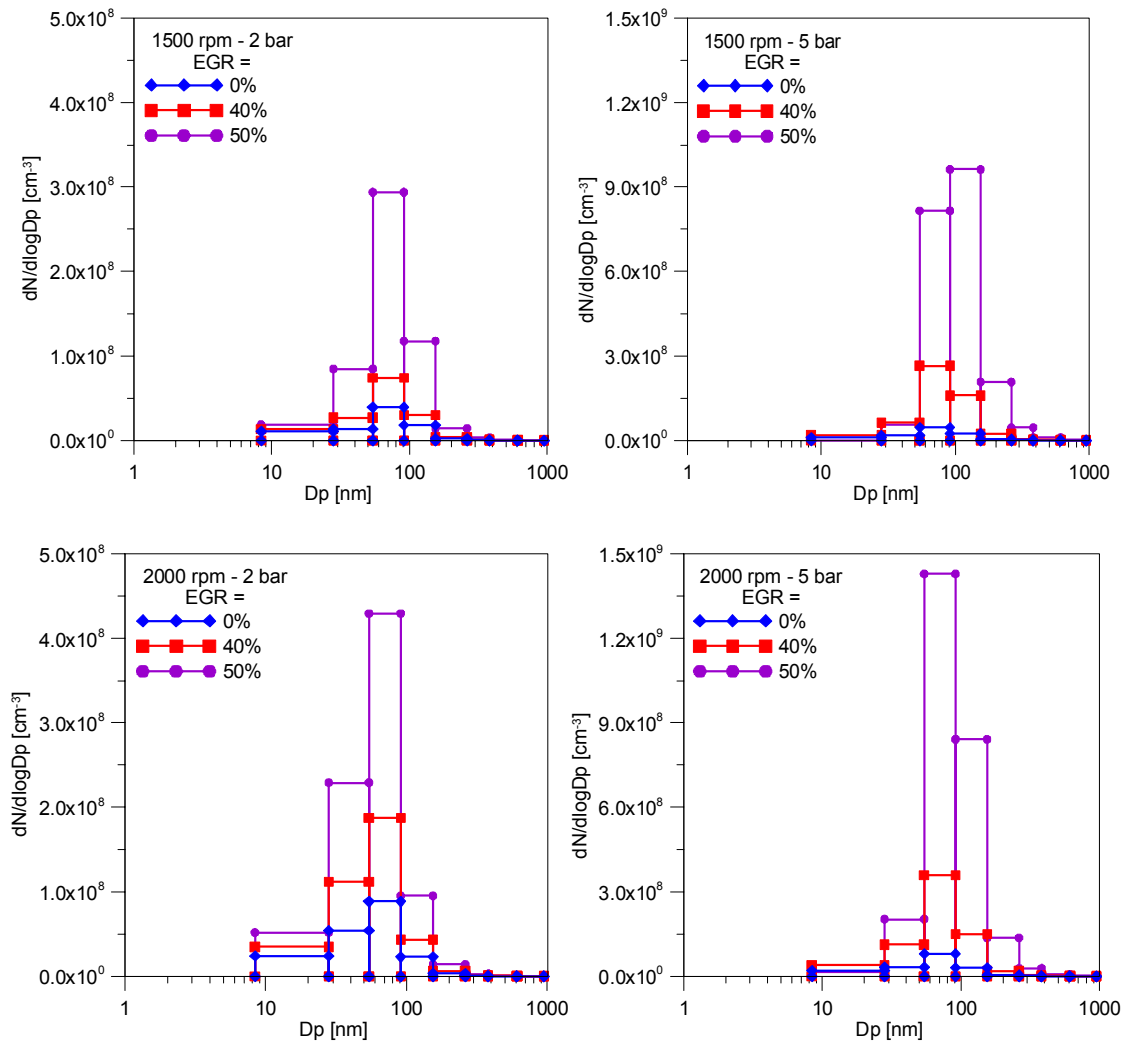


Figure 4.5. Particles size distributions obtained by ELPI.

For both speeds and loads, the number concentration of particles bigger than 54 nm with respect to the total number increased. On the other side, the fraction of particles impacted on the ELPI first and second stages ($D=7-54\text{nm}$) was reduced at higher EGR. This result was partially due to the reintroduction of smaller particles contained in the exhaust gases into the cylinder. These particles represented nuclei for the agglomeration of particles in the accumulation mode.

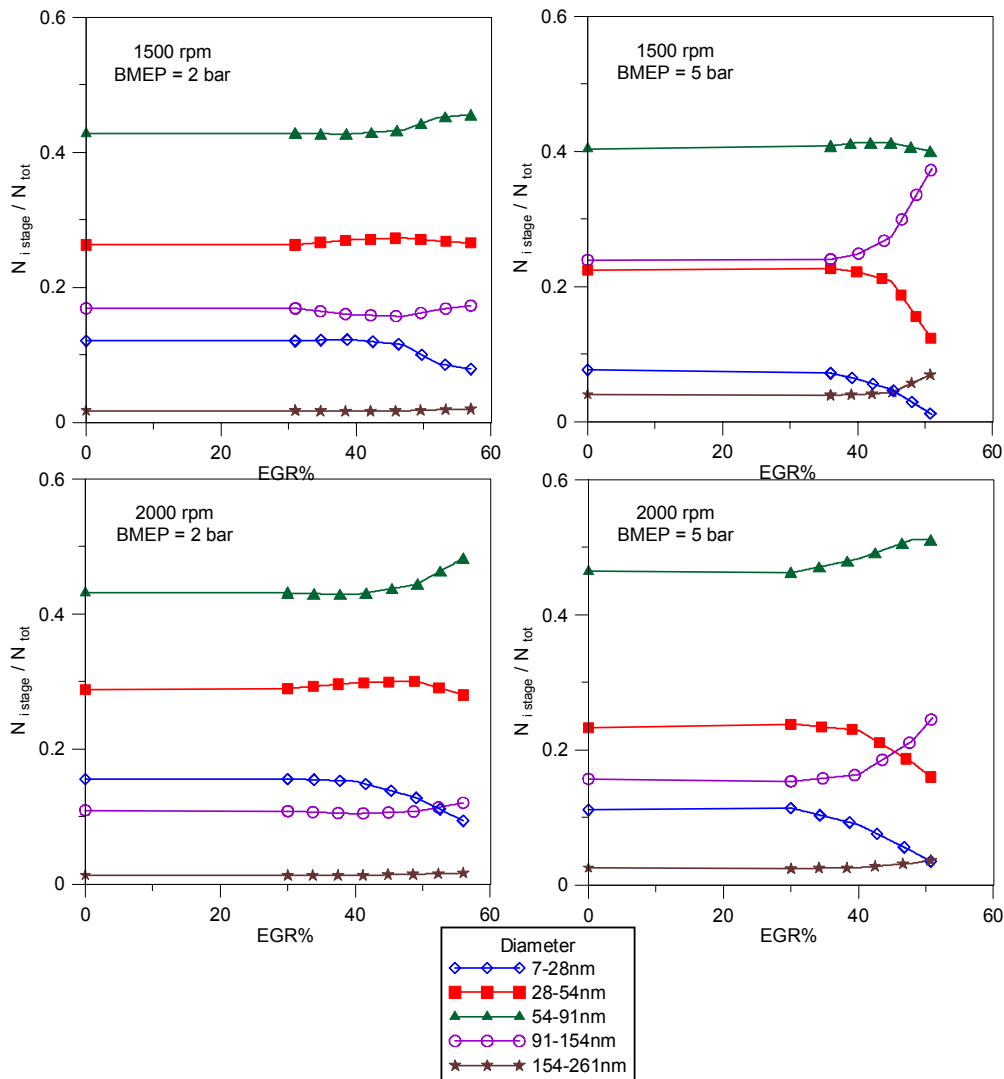


Figure 4.6. Effect of EGR on the number of particles size collected by ELPI in the first stages.

4.2.3. Effect on primary particles size and chemical nature by LII and BUVESS measurements

In order to evaluate the effect of EGR on soot primary particles, Laser Induced Incandescence (LII) was applied at the raw exhaust. In Figure 4.7 the LII mean diameters are reported. For all the engine conditions, it can be noted that no primary particles smaller than 20 nm were measured.

With respect to EGR variation, for all the conditions from 30% of EGR the diameters gradually increased. The trends obtained by LII and ELPI are similar; this means that an

increase of primary particles diameter corresponded to aggregates mean size growth. This effect was probably due to the introduction of soot in the combustion chamber.

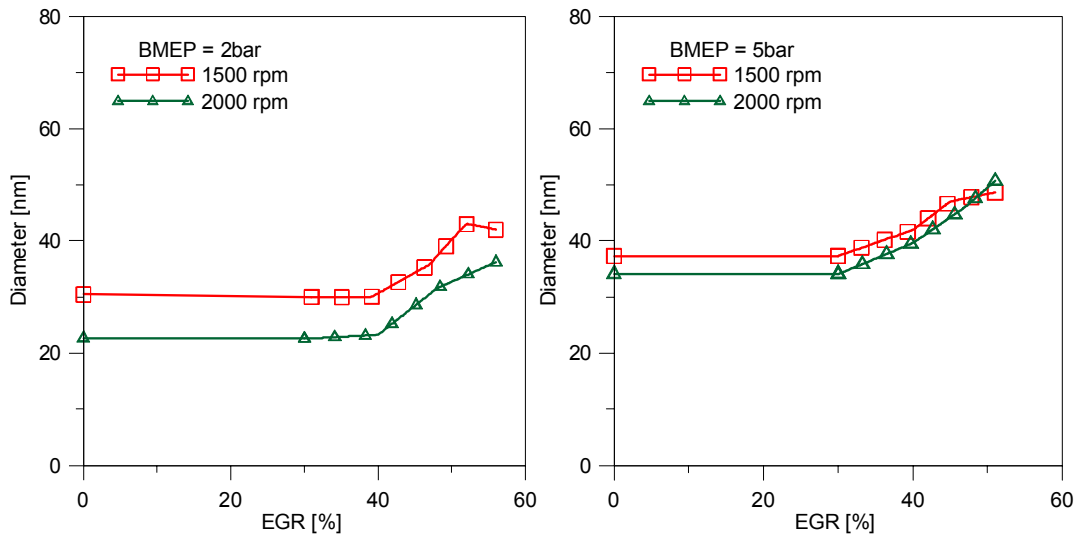


Figure 4.7. Particles diameter measured by LII for different EGR.

Particles in the combustion chamber can go by two different routes: the first one consists in a complete oxidation with CO_2 and H_2O formation. The second one is characterised by a not complete oxidation. In this case, soot is partially oxidised [121] and the resulting structures can become nuclei for the following superficial growth. At this point particles can be emitted directly at the exhaust or follow the coagulation process. The results obtained by LII measurements, seem to state that the second path predominates on the first one; as a consequence, bigger primary particles are formed [55]. A sketch of the possible primary particles formation mechanism is reported in Figure 4.8. However, the increasing in primary particles diameter could also be caused by the low oxidation rate of soot at high EGR% due to a reduction of oxygen concentration. Unfortunately, the numerical analysis of these phenomena is very complex due to the coexistence of gaseous-vapour-liquid and solid phases.

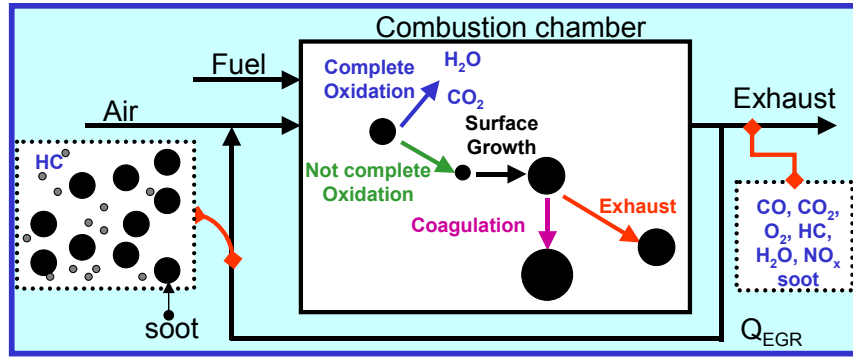


Figure 4.8. Evolution of soot primary particles in the combustion chamber as effect of EGR.

To evaluate the effect of EGR on chemical nature of particles and on their size distributions, Broadband UV–Visible Extinction and Scattering Spectroscopy (BUVESS) technique was applied [75]. Particle size distributions obtained by the numerical procedure previously described are reported in Figure 4.9.

For all the engine operating conditions, the best agreement between experimental and theoretical BUVESS spectra was obtained using soot optical properties reported in ref. [82]. In particular, the emitted material showed a refractive index similar to flame-soot one, with low level of graphitisation. For both engine speeds, at BMEP=2 bar and no exhaust gas recirculation, a unimodal size distribution with mean diameter around 20 nm was measured. These particles were produced by the chemical interaction of soot precursors formed in the combustion chamber. At increasing EGR% value, a bimodal distribution was observed. The second mode was due to the particles reintroduced in the combustion chamber together with the exhaust gases; they represented nuclei for the further growth. These results agree with LII measurements. At BMEP=5 bar and no exhaust gas recirculation, a bimodal size distribution was evaluated. The accumulation mode in the absence of EGR, could be due to the overall mixture richness that promoted the surface growth, coagulation and coalescence of the nucleation particles reintroduced

in the combustion chamber. At increasing EGR%, a strong increase of number concentration and mean size of accumulation particles was observed.

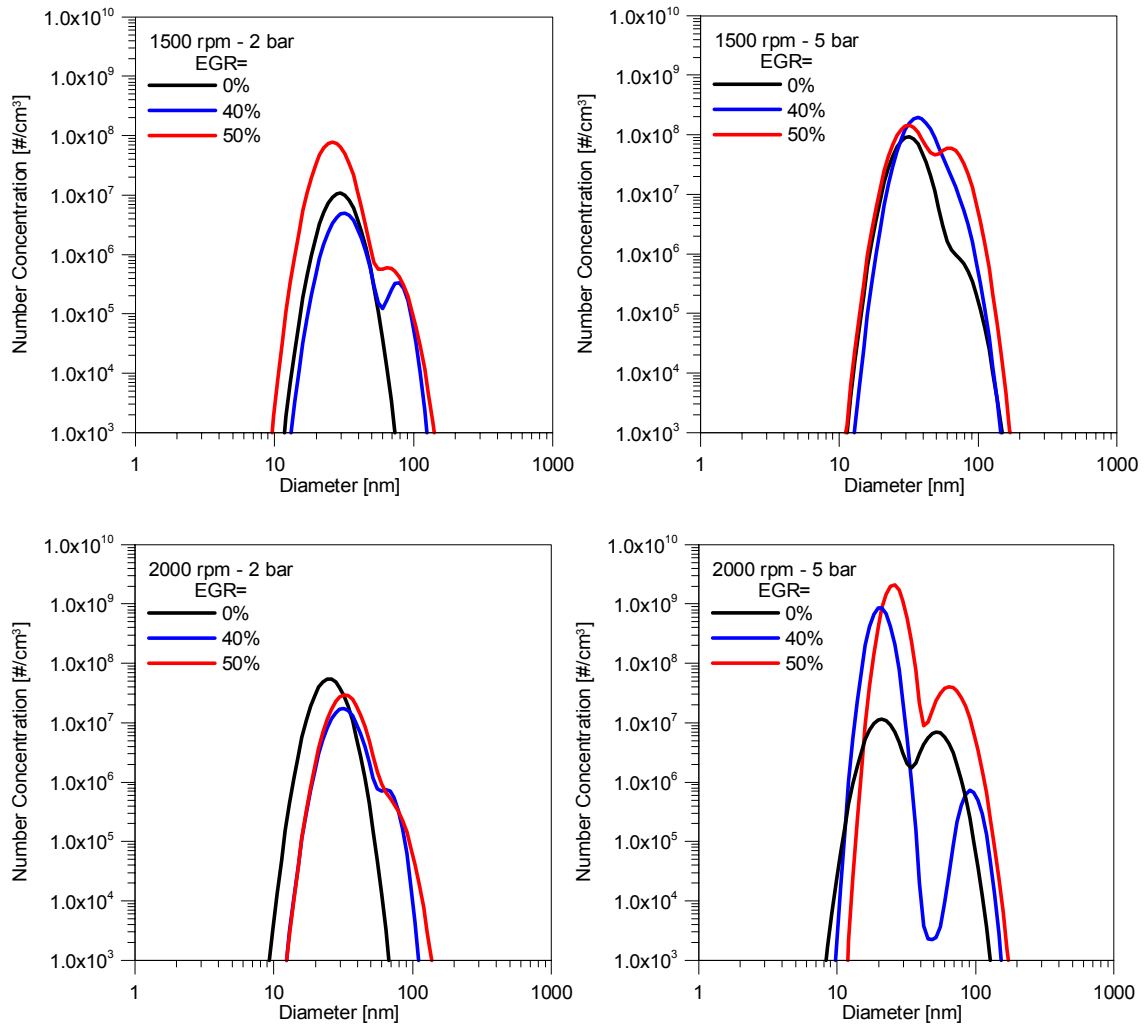


Figure 4.9. Particles size distributions obtained by BUVESS for the selected operating conditions.

In conclusion the recirculation of exhaust in the combustion chamber didn't modify the chemical properties of the particles. On the other hand, the EGR had a physical effect on the emitted nanoparticles; in fact it induced the formation of an accumulation mode in the size distribution [122, 123].

4.3. Catalysed Diesel Particulate Filter

4.3.1. Loading phase

Catalysed Diesel Particulate Filters remove the particulate matter from engine exhaust collecting it on the filter layers. If the temperature inside of the filter is below the regeneration one, the catalyst is not active and the CDPF acts as a physical filter (loading phase). During the loading phase the backpressure increases and the filtering efficiency can be higher than 90% in terms of mass concentration as well known by literature [124]. On the other hand, poor information about the effect of the CDPF can be found on the nanoparticles emitted during the loading phase in terms of size distribution and chemical nature. To improve the knowledge of this effect, BUVESS measurements were carried out upstream and downstream of the filter for the optimised engine operating conditions and at different EGR values.

Figure 4.10 shows the effect of the filter on the particles size distribution at 2000 rpm - 2 bar at different EGR. The particle number concentration was reduced by approximately 2 orders of magnitude by the filter, but the shape of the distribution remained approximately the same. Moreover, the best agreement between experimental and theoretical BUVESS spectra was obtained using soot optical properties both upstream and downstream of the filter. No change was observed in the nanoparticles chemical nature during the crossing of the CDPF since the catalyst was inactive and the filter had only a physical effect.

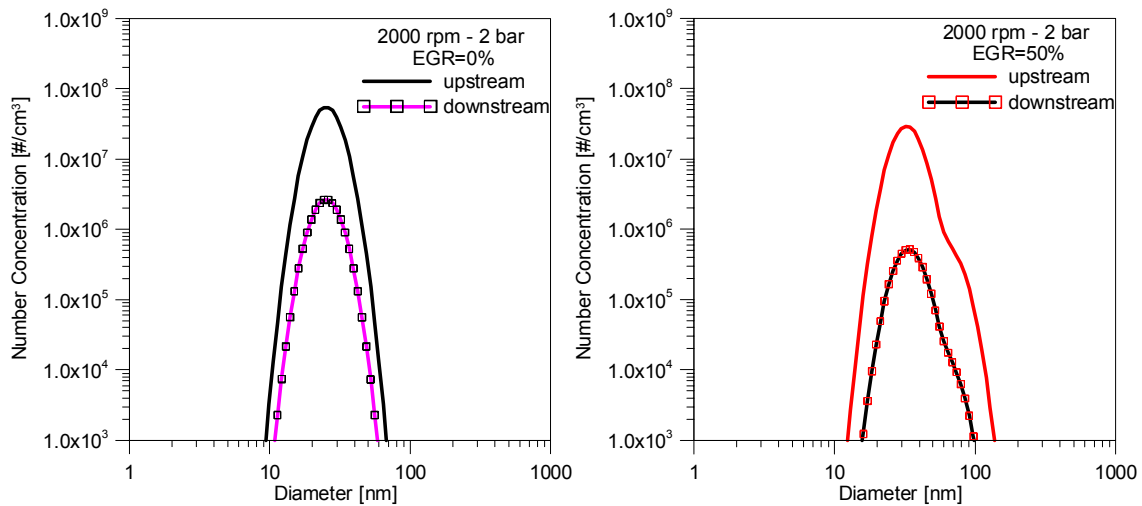


Figure 4.10. Particles size distributions obtained by BUVESS.

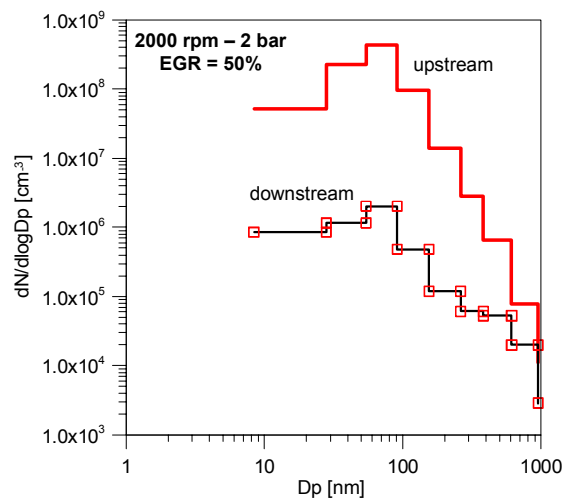


Figure 4.11. Particles size distributions obtained by ELPI.

In figure 4.11 the size distributions obtained by ELPI measurements upstream and downstream of the CDPF at 2000 rpm - 2 bar and EGR = 50% (optimised value) are reported. The ELPI results showed a reduction of the particles number concentration through the filter by approximately 2 orders of magnitude in good agreement with BUVESS. These measurements confirmed that the filter during the loading phase didn't affect the particles distribution shape but it acted only on the number concentration.

4.3.2. Regeneration Phase

In order to analyse the process of CDPF regeneration [10], the accumulation of 7 g of particulate matter was carried out starting from the empty filter. The CDPF was regenerated fixing the engine speed at 3000 rpm and the load at 12 bar (corresponding to 54 kW). During the regeneration, the engine remained stable in terms of O₂ concentration at the exhaust (8% vol) and equivalent air-fuel ratio (1.6).

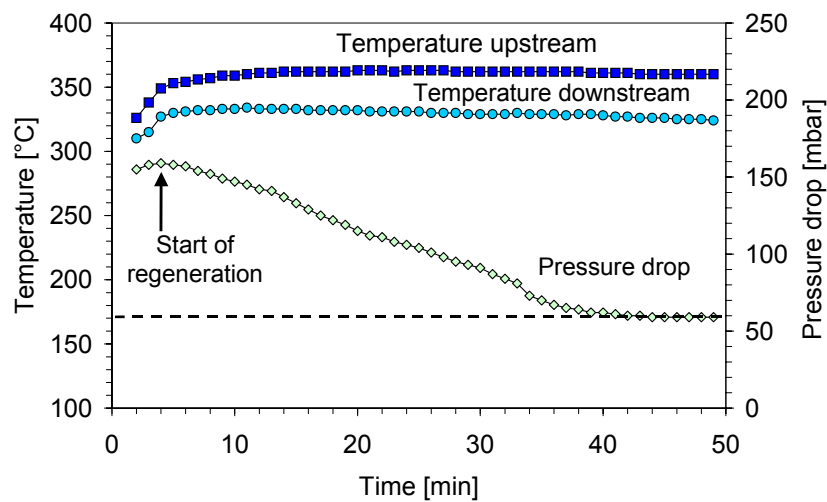


Figure 4.12. Pressure drop of CDPF and temperatures measured upstream and downstream the CDPF.

In Figure 4.12, temperature values measured upstream and downstream of the CDPF and the pressure drop during the regeneration process are reported. When the temperature upstream of the CDPF reached 350°C, regeneration phase took place and the pressure drop (ΔP) started decreasing. The regeneration stopped when a steady value of ΔP was reached. When filter was empty the measured pressure drop was 60 mbar for the selected operating condition.

Mass concentration of particulate matter upstream and downstream of the CDPF is reported in Figure 4.13a. The mass filtering efficiency, defined as:

$$Efficiency\% = \frac{particulate \cdot mass^{IN} - particulate \cdot mass^{OUT}}{particulate \cdot mass^{IN}} \times 100$$

resulted negative approximately from 10 minutes after the beginning of the regeneration until the end. Thus the filter seemed to emit a fraction of the previously stored particulate matter. This result was probably due to the opacimeter sensitivity not only to particles, but also to several gaseous hydrocarbons. This hypothesis was confirmed by HC and mass concentration trends, shown in Figure 4.13.

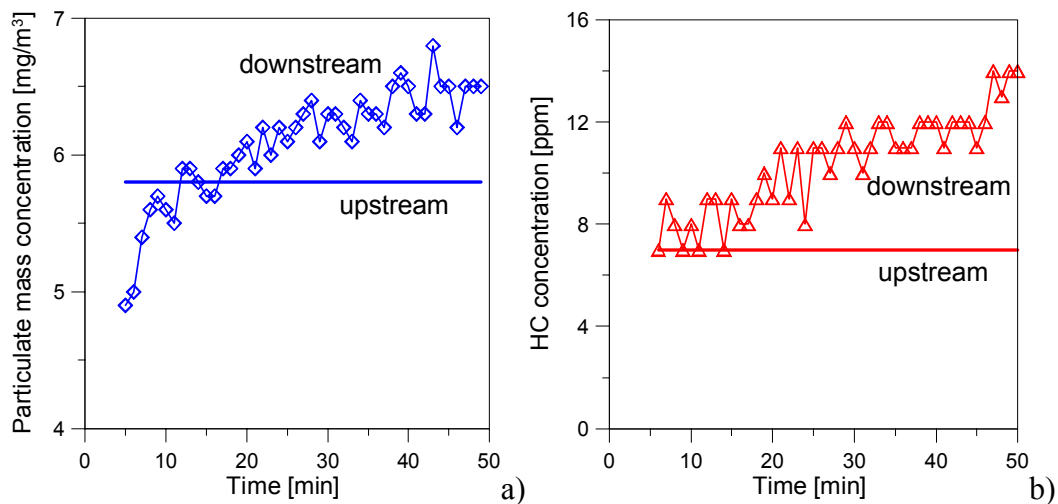


Figure 4.13. Evolution of particulate mass concentration (a) and HC concentration (b) during the regeneration phase.

In order to have information about particles number concentration and the chemical nature of emitted particulate, broadband extinction and scattering measurements were carried out upstream and downstream of the CDPF.

A comparison between a spectrum detected upstream of the filter and the theoretical one obtained using soot optical properties is reported in Figure 4.14a. The average discrepancy is lower than 10%. The corresponding number size distribution is unimodal (Figure 4.14b) with particles mean size around 20 nm, it is in agreement with the results reported in literature [125].

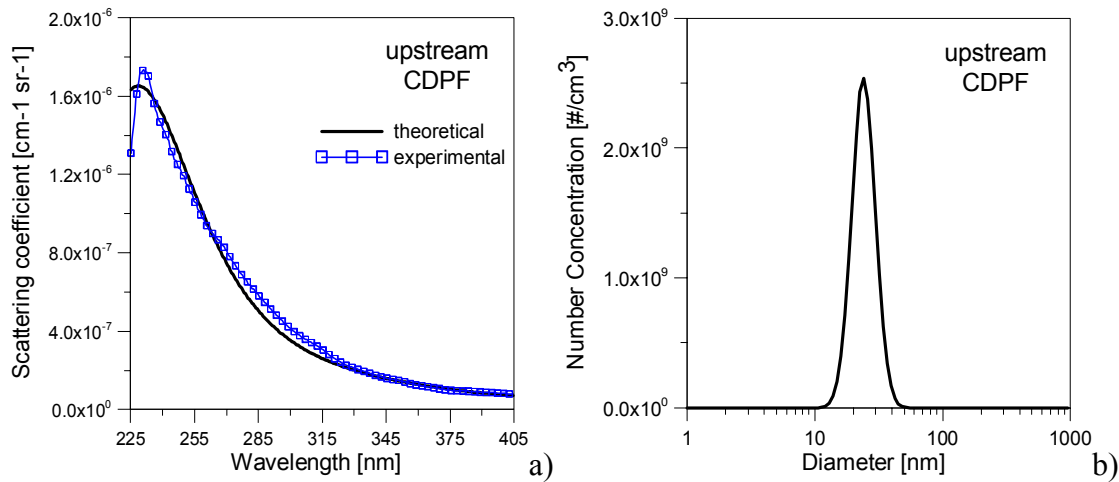


Figure 4.14. Experimental and theoretical spectral scattering coefficients (a) and particle number concentration (b) upstream of the CDPF.

Analogous optical investigation was realized downstream of the filter at 10 minutes during the regeneration. A unimodal size distribution was obtained considering soot optical properties. The number concentration was higher than upstream and the mean diameter was around 10 nm (Figure 4.15a). In this case, high number of nanoparticles smaller than 10 nm was revealed. They could come from the fragmentation of the micronic external layer of the soot cake. As a consequence the numerical filtering efficiency was negative in the size range sub-30 nm.

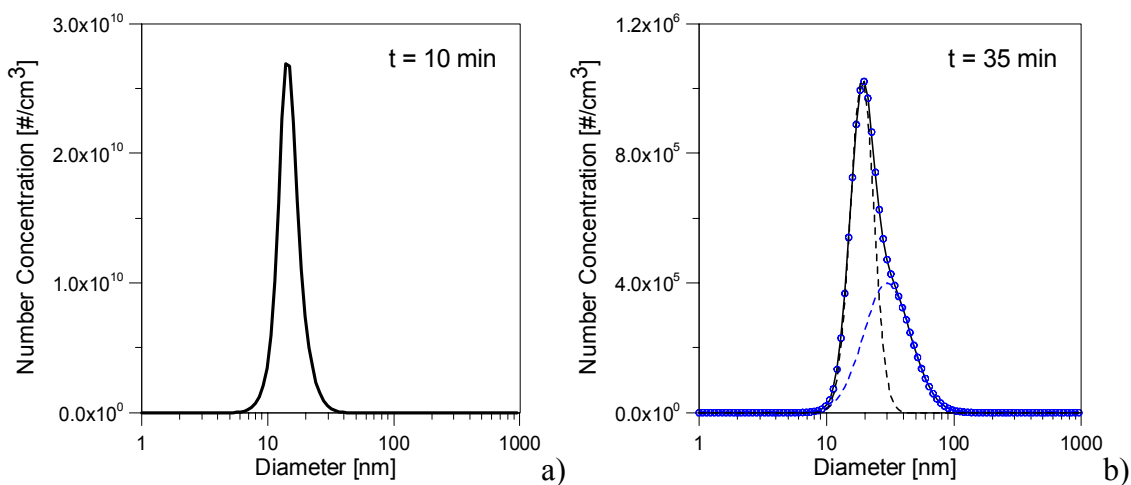


Figure 4.15. Particle number concentration downstream of the CDPF at 10 minutes (a) and 35 minutes (b).

Until 30 minutes, unimodal distributions were measured. After this time, at 35 minutes, two particles modes were observed as reported in Figure 4.15b. The bimodal size distribution pointed out two classes of particles with mean diameters of 15 nm and 30 nm respectively. The best agreement between theoretical and experimental scattering spectra was obtained using a volume mixture [85] of NOC and soot for the first mode, and soot optical properties for the second one. At this point of regeneration, the number of particles resulted lower than upstream by 3 orders of magnitude. The particles stored in the filter were burnt and consumed so the result was a small number of particles and high concentration of hydrocarbons.

An analysis of number filtering efficiency weighted on particle size showed negative values with respect to diameters smaller than 10 nm for the whole regeneration phase, as reported in Figure 4.16. The effect of this drop is the emission in the atmosphere of very high number concentration of nanometric particles. Due to the low sticking coefficient of nanoparticles they remain in atmosphere for long time with negative effects on human health [126].

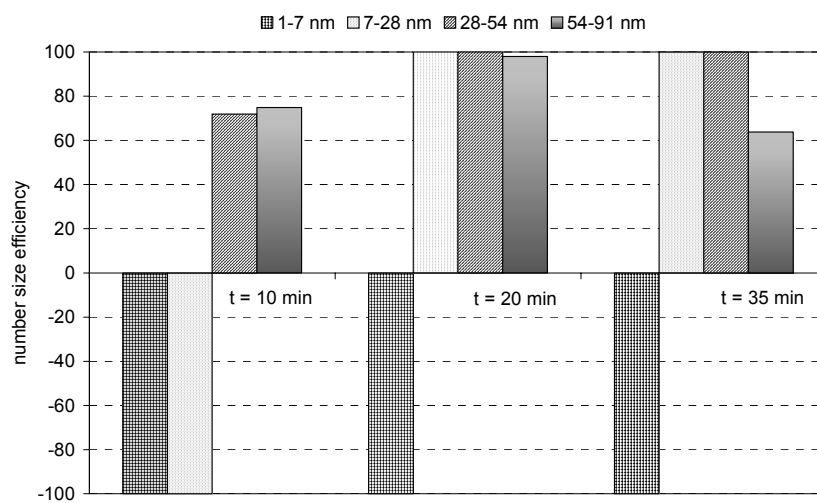


Figure 4.16. Number size efficiency of the CDPF during regeneration.

Chapter 5:

EXPERIMENTAL RESULTS: SPARK IGNITION ENGINE

5.1. Engine Operating Conditions

Several experimental techniques were applied at the exhaust of a Port Fuel Injection Spark Ignition (PFI SI) engine equipped with a three-way catalyst (TWC) in order to characterise the particles emission. The engine was operated in steady state conditions at different speeds and loads. Each operating condition was maintained for 10 minutes, allowing the stabilization of the engine. Table 5.1 reports the details of engine operating conditions and the value of λ (air-to-fuel ratio value with respect to the stoichiometric one).

Speed [rpm]	Load [%]	Bmep [bar]	Fuel [kg/h]	λ
1500	50	8.7	3.6	1.0
1500	100	8.9	3.7	1.0
2000	50	8.5	4.8	1.0
2000	100	9.2	5.3	0.9
3000	50	9.1	7.5	1
3000	100	9.5	7.8	0.9
4000	50	9.5	11.8	0.9
4000	100	10	12.1	0.9

Table 5.1. Engine operating conditions.

To gain further insights into the particles formation and emission mechanisms, the measurements were performed both upstream and downstream of the catalytic converter.

5.2. Three way catalyst effect on engine emissions

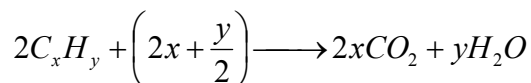
The effect of the three-way catalyst on the engine emissions was evaluated by means of conventional measurements of gas concentration and opacity and by means of the Electrical Low Pressure Impactor (ELPI). The exhaust gas concentrations were obtained by fast analysers. NO_x was measured by an electrochemical sensor, HC and CO by infrared analysers NDIR (No-Dispersive Infrared Detectors).

The three-way catalytic converter has three simultaneous tasks:

Reduction of nitrogen oxides to nitrogen and oxygen: $2NO_x \longrightarrow xO_2 + N_2$

Oxidation of carbon monoxide to carbon dioxide: $2CO + O_2 \longrightarrow 2CO_2$

Oxidation of unburned carcinogenic hydrocarbons (HC) to carbon dioxide and water:



In the figures 5.1 - 5.3 the NO_x, HC and CO concentrations upstream and downstream of the three way catalyst are reported. As expected [127], a very high conversion efficiency was measured as shown in Figure 5.4.

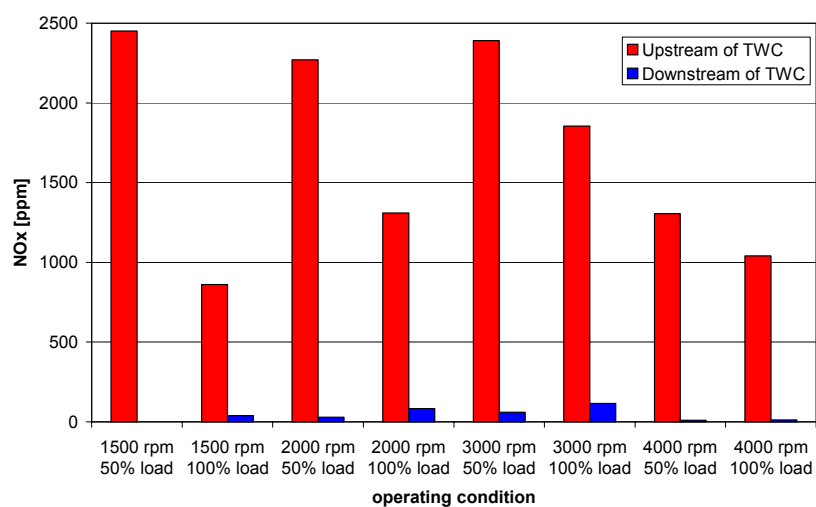


Figure 5.1. NO_x concentration upstream and downstream of the TWC.

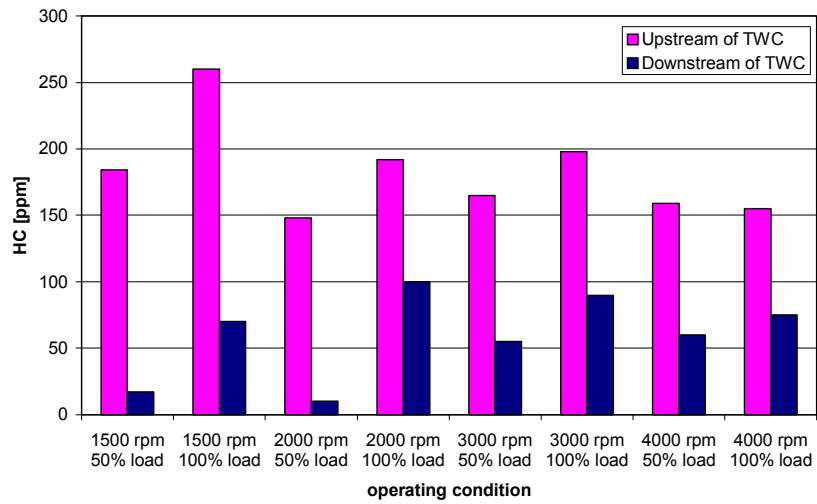


Figure 5.2. HC concentration upstream and downstream of the TWC.

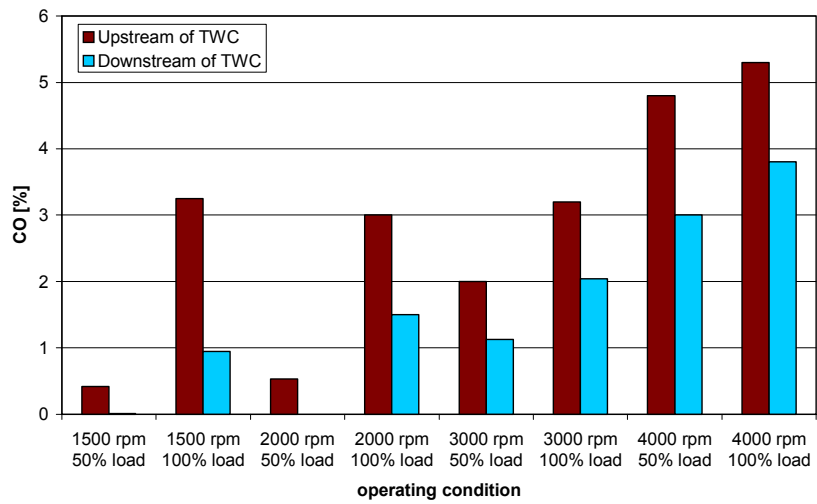


Figure 5.3. CO concentration upstream and downstream of the TWC.

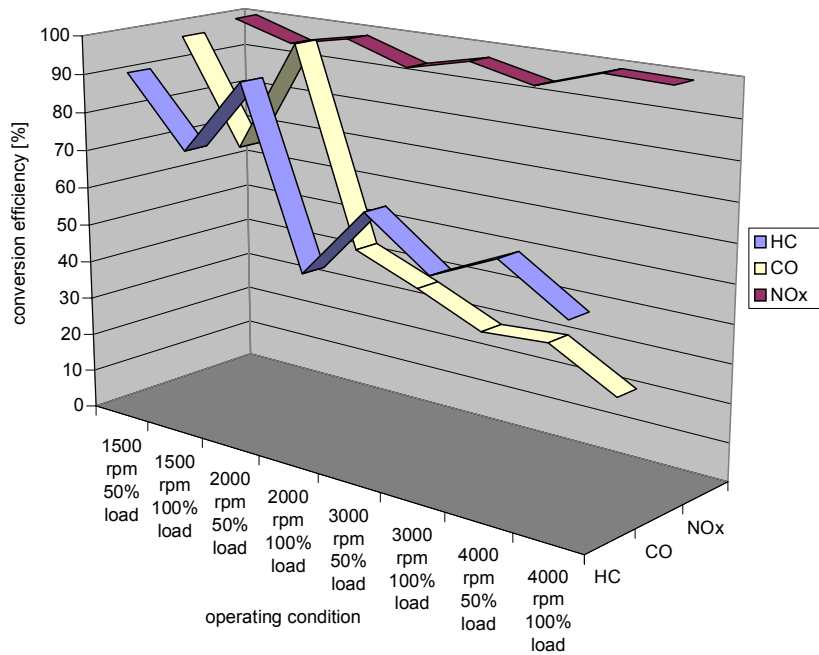


Figure 5.4. NOx, HC and CO conversion efficiency through the TWC for the selected operating conditions.

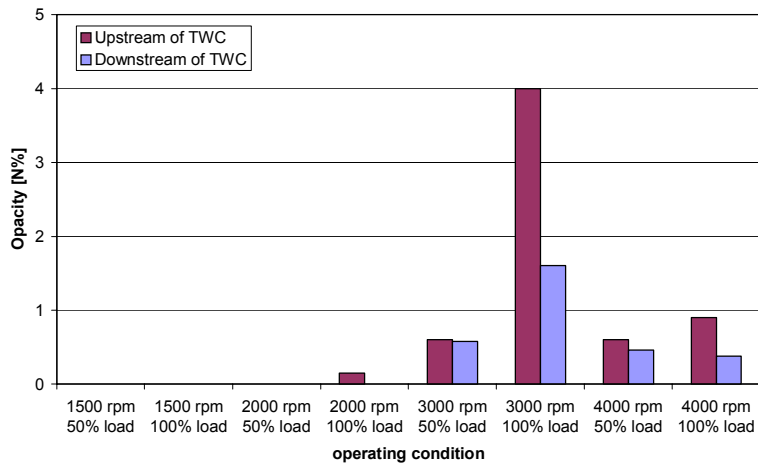


Figure 5.5. Opacity of the exhaust gases upstream and downstream of the TWC.

In the selected engine conditions the opacity of the exhaust was measured using an opacimeter. The results are reported in Figure 5.5. A value of opacity different from zero upstream of the TWC was evaluated at 3000 and 4000 rpm and at 2000 rpm 100%

load. In all these conditions, the measurements performed downstream the TWC showed a reduction in opacity.

The opacimeter is widely used for the particulate mass concentration measurements [128] especially at the exhausts of diesel engines; nevertheless this instrument shows several limits. Its operating principle is the visible light (green) attenuation in the exhaust stream. Among the particulate matter components, soot is recognized as the main substance responsible for the opacity, and therefore, opacimeters usually convert their measurements into soot concentrations [129]. On the other hand, some hydrocarbons (SOF) adsorbed on the particles surface or simply emitted as liquid droplets are able to absorb light at the same wavelength. In addition, other emitted gases, such as NO , NO_2 , SO_2 and H_2O vapour, participate in the light absorption, leading to an extra light extinction as reported in literature [130, 131]. Moreover the opacimeter shows low sensitivity to small particles. As demonstrated by the electromagnetic theory, particles of 200 nm in diameter or greater block green light in proportion to their cross-section surface area. Nevertheless, particles of 50 nm in diameter block only about 15% of their surface area. This means that opacity data depend on particle sizes and they will underestimate the number concentration if smaller particles are present [132].

Since NO_x and HC concentrations were strongly reduced by the TWC, the interaction between opacity and those gases was slight in the “downstream flow”. On the other hand, the results achieved upstream of the TWC could be biased from the gas composition. In any case, the opacimeter is able to give information only about particulate mass concentration and it shows several limits as above explained. Thus, a further investigation was necessary to obtain information on the TWC effect on the

particles emission. For this reason, ELPI measurements were carried out, the results are reported in Figure 5.6

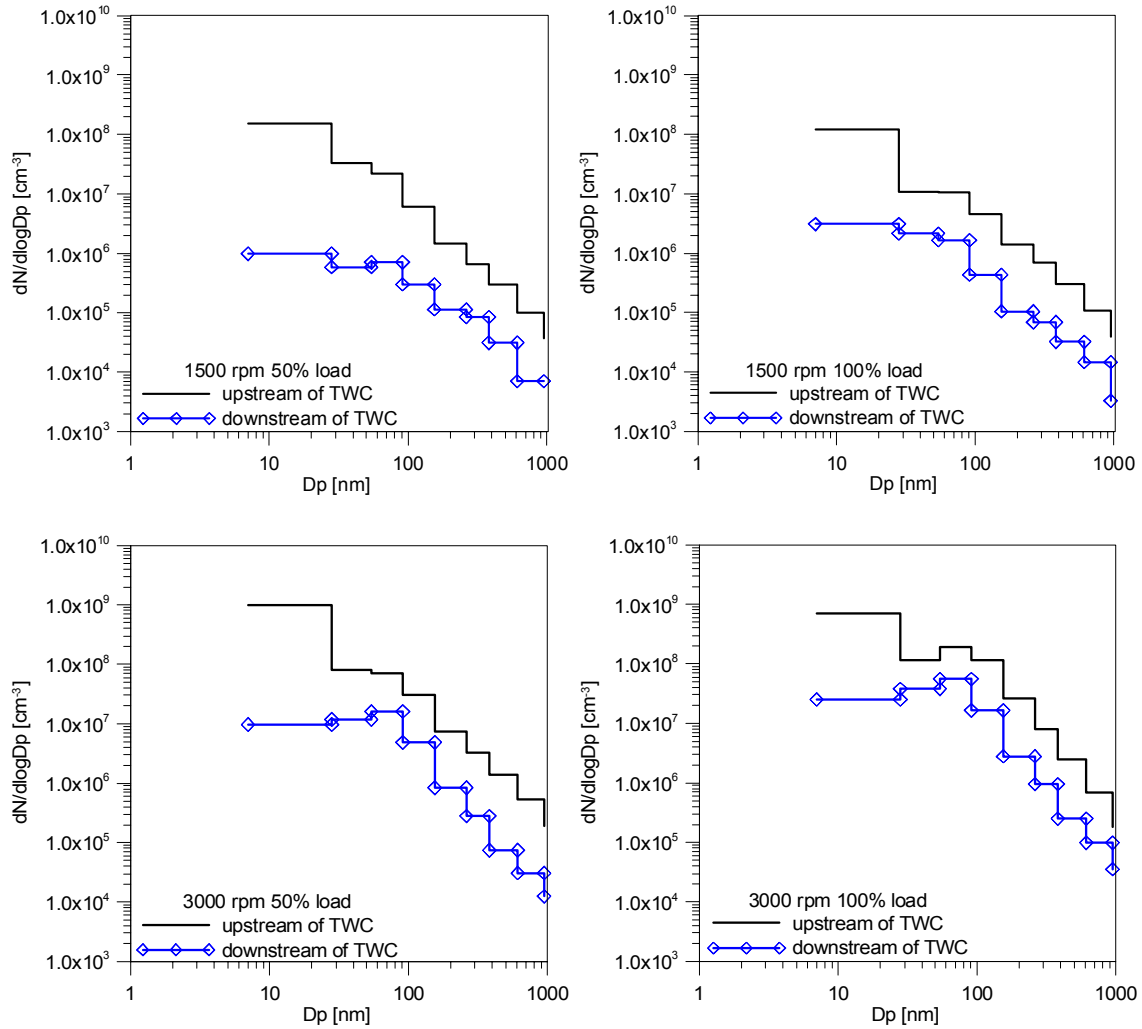


Figure 5.6. Particle number concentration measured by ELPI upstream and downstream of the TWC.

The exhaust particles in the “upstream flow” constituted a single mode size distribution with highest number concentration at the first impactor stage in the range 7-28 nm.

It is possible to observe an overall reduction in number concentration of 1-2 orders of magnitude when the exhaust gas passes through the TWC.

The primary mechanism for the “removal” of these particles is probably catalytic stripping of volatile hydrocarbon particle precursors (diffusive particle loss within the catalyst is low for particles larger than 10 nm) which are still in the gas phase at exhaust temperatures [133]. By stripping these gas phase hydrocarbons, the catalyst is removing material which would have otherwise nucleated to form volatile particles during the dilution process [34].

The effect of particle precursor removal by the catalyst is clearly seen through the size distributions presented in Figure 5.6. When compared with the upstream particle size distribution, the downstream size distribution shows a stronger decrease in the number of particles smaller than 30 nm. This reduction in small particles is expected if the main mechanism for particle reduction by the catalyst is the volatile precursor stripping. In fact the particles formation through nucleation of volatile gas phase precursors tends to produce small particles.

The nucleating gas phase heavy hydrocarbons can come from the break-up of intake valve and combustion chamber deposits. As these deposits break up, the hydrocarbons which had been adsorbed upon them are released and volatilized. This produces a localized region of hydrocarbon supersaturation, resulting in nanoparticles formation through homogeneous nucleation [15].

Figure 5.6 shows that the number of larger particles is decreased downstream of the catalyst as well. The most likely mechanism for removal of these larger particles (which due to their size and probable composition are likely to be in a solid particulate phase in the exhaust) is inertial impaction at the catalyst channel faces [34].

Even if the TWC reduced the number concentration of approximately two orders of magnitude, high number of nanoparticles was measured at the engine exhaust. Due to

their small mean volume, the corresponding mass was very low and within current normative [134]. On the other hand, they could represent a problem in order to respond to future stringent emission legislation.

5.3. Characterisation of the particles downstream of the TWC

5.3.1. Optical techniques (BUVESS and LII)

As observed from ELPI results, low particles number concentrations were detectable at PFI SI engine exhaust downstream of the three-way catalyst. In this condition the optical techniques result a very powerful sizing methodology: they are real time, “in situ” and non-intrusive techniques and they allow the characterization of primary particles in terms of size distribution and chemical nature also at very low number concentrations.

Laser Induced Incandescence (LII) and Broadband UV–Visible Extinction and Scattering Spectroscopy (BUVESS) were applied at the undiluted exhaust of the engine, downstream of the TWC. Laser Induced Incandescence measurements were performed to detect and size carbonaceous particles. A well resolvable LII signal with respect to noise was revealed only at high speeds (3000 and 4000 rpm).

According to the relations reported in the LII theoretical background, carbonaceous particles mean diameters resulted in the range 30-60 nm, in good agreement with literature [135]. (Figure 5.7). The presence of this kind of particles at the port fuel injection spark-ignited engine exhaust concurs with recent studies [136]. In port fuel injection spark-ignited engines, thin films of liquid fuel can form on the valves surface and on the cylinder walls [137-141]. Once formed, the fuel films develop dynamically under the influence of gas flow and valve movement and they affect the complexity of

the combustion process. In particular, film vaporization and fire near the valves can reduce the flame speed and the complete flame propagation creating locally rich-zones. During the fuel film-evolution process, it is possible to achieve gas temperature and mixture strength conditions that lead to fuel film ignition, creating a diffusion-controlled flame that can persist well after the normal combustion event. Just before the opening of the exhaust valves, this flame produces soot which cannot be completely oxidized due to the too low temperatures in the cylinder. Chamber locations where the fuel-air mixture is too lean to burn are a particular concern for unburned hydrocarbon emissions. Thus, the fuel film burning leads to increased smoke and hydrocarbons emissions [142].

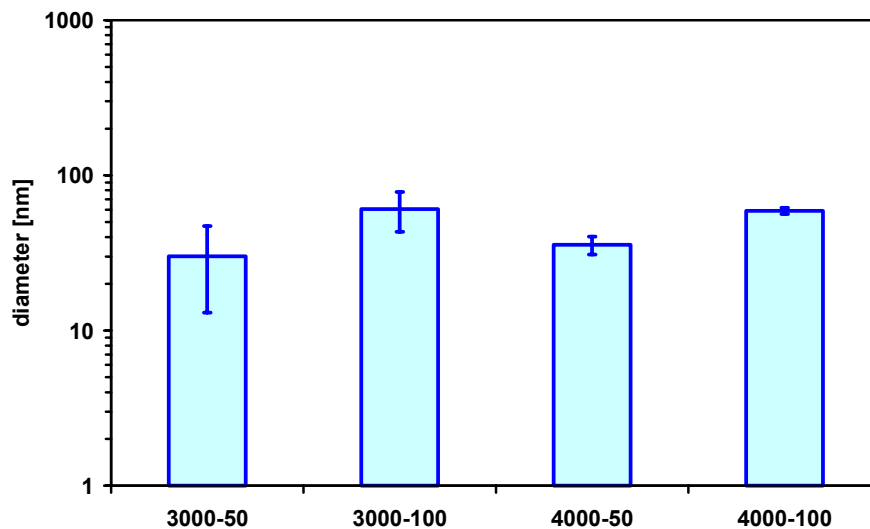


Figure 5.7. Mean diameters of carbonaceous particles obtained by LII.

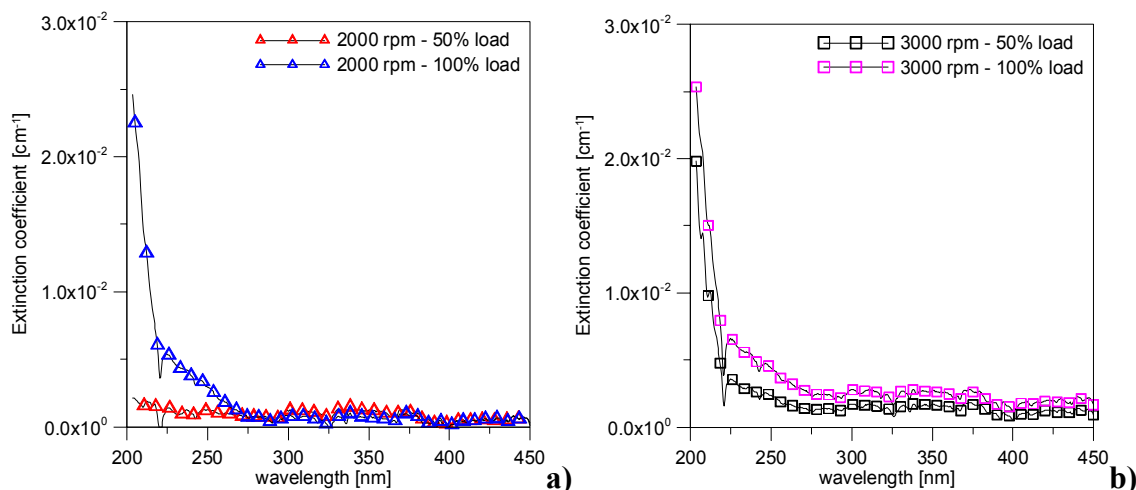


Figure 5.8. Spectral extinction coefficients measured at (a) 2000 rpm and (b) 3000 rpm at 50% and 100% load.

In order to investigate the whole range of engine operating conditions and to evaluate the chemical-physical nature of particles also at low engine speeds, BUVESS measurements were performed.

Figure 5.8 shows the spectral extinction coefficients measured at (a) 2000 rpm and (b) 3000 rpm. As previously discussed, at low engine speed LII didn't detect carbonaceous particles; this occurred only for engine speed higher than 2000 rpm. In all the investigated cases, the coefficients show an increasing intensity at increasing load. Moreover, a broad and less intense band in the range 300 - 400 nm was observed. It could be due to the presence of 3-4 rings aromatic hydrocarbons [143].

For all the conditions except for low engine speeds and low load, the extinction spectra show a strong UV band below 220 nm. It can be related to the simultaneous presence of carbonaceous material and one-two rings aromatic hydrocarbons [143]. In the same conditions the spectra present a continuous contribution that decreases with wavelength dependence like λ^{-1} . This spectral behaviour can be considered a marker of nanoparticles according to Mie theory in the Rayleigh approximation [74].

In Figure 5.9 the spectral scattering coefficients measured at the selected operating conditions are reported. At higher speed (Figure 5.9 b) scattering coefficients with analogous spectral behaviours were detected, they differed in terms of intensity. This results indicates the similar chemical-physical nature of the emitted particles. In these conditions scattering coefficients increased with λ^{-4} wavelength dependence in the deep UV, below 300 nm. This spectral feature is typical of very small carbonaceous particles in Rayleigh regime [74].

At 1500 and 2000 rpm, the scattering coefficients were lower in intensity than higher speed conditions and they showed different spectral behaviours. In particular, the spectra seem to change from 1500 rpm – 50% load to 2000 rpm –100 % load until a spectral behaviour comparable with that measured at 3000 rpm – 50% load. For all the spectra reported in Figure 5.9a, an intense band below 300 nm was observed. This band cannot be correlated with the scattering of carbonaceous particles even if a very small diameter (<15 nm) is considered. At increasing speed and load, the band is included in a continuous broad band that simultaneously rises and covers the whole spectral range. This band seems to indicate an evolution of the chemical nature of particles until the carbonaceous ones in Rayleigh regime observed at higher speeds.

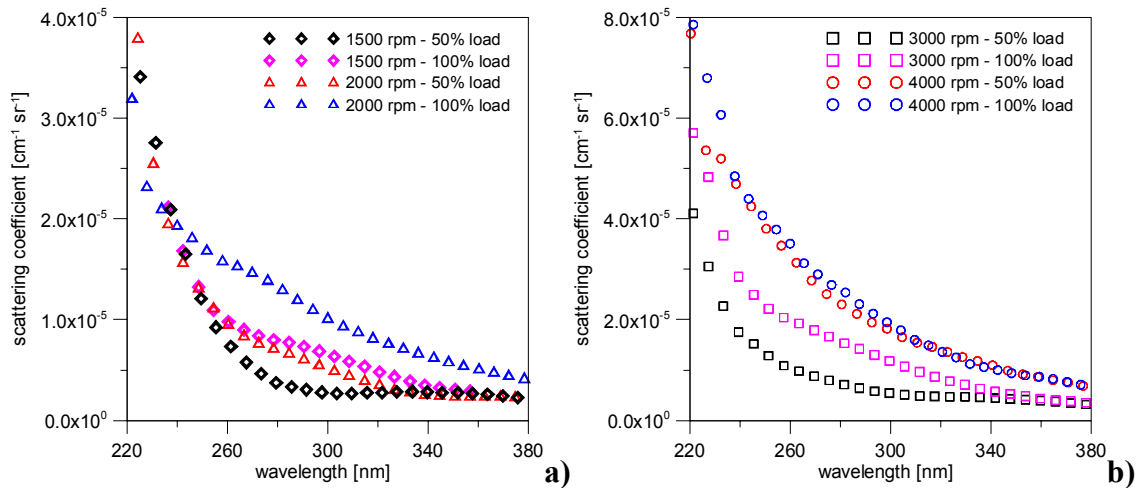


Figure 5.9. Spectral scattering coefficients measured at the selected operating conditions.

In order to achieve information about the size distributions and the properties of the particles from the optical measurements, the retrieving procedure described in the theoretical background was applied.

A comparison between the experimental and theoretical Mie scattering spectra at 3000 rpm and 50% load and at 4000 rpm and 100% load is reported in Figure 5.10. The agreement was obtained by the size distributions reported in Figure 5.11.

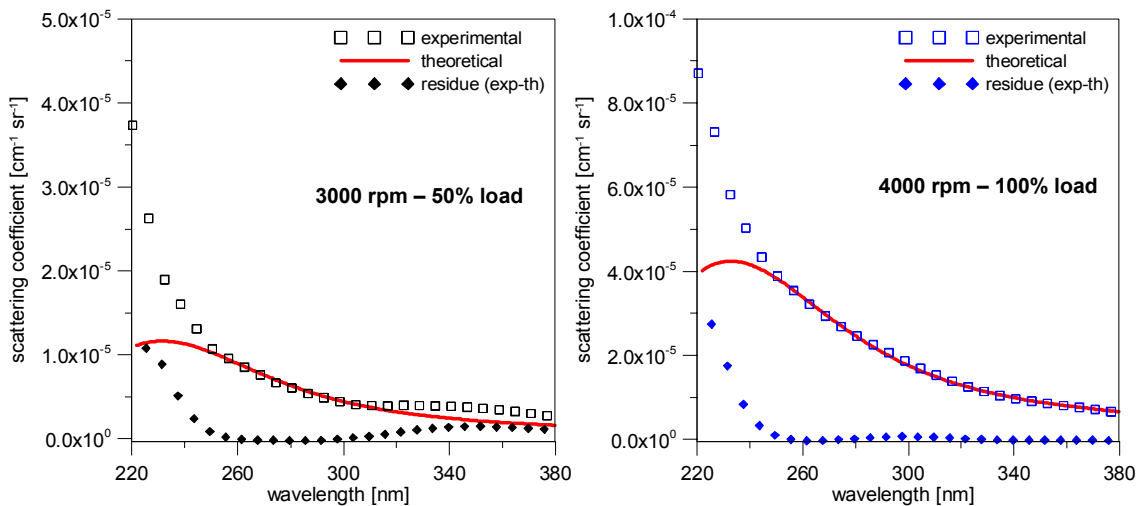


Figure 5.10. Experimental and theoretical spectral scattering coefficients.

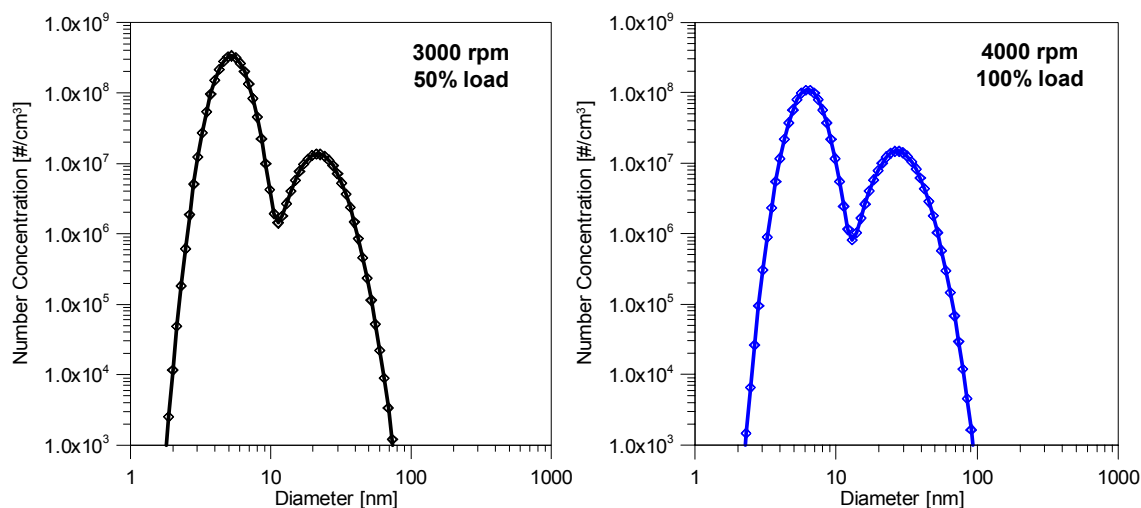


Figure 5.11. Particles size distributions obtained by BUVESS.

Two particles modes were evaluated by the numerical procedure: the first one was composed by particles with 30 nm mean diameter and the soot optical properties reported in ref [82]. The Mie scattering spectrum related to this class of particles reached an agreement with the experimental data in the range 300 nm – 380nm with a mean discrepancy lower than 10%. The numerical procedure identified a second mode in order to improve the agreement between experimental and theoretical spectra especially for wavelengths below 300 nm. This mode was characterised by particles with mean diameter below 10 nm and the optical properties of NOC reported in ref [83]. Its contribution to the Mie scattering spectrum was very small if compared to the other mode and it allowed reducing the discrepancy of 3-5%.

In order to better understand the nature of all the species emitted at the exhaust, the residue obtained by the difference between experimental and theoretical spectra was evaluated for all the selected conditions. A residual scattering below 260 nm was well resolvable as reported in Figure 5.10 and comparable results were attained for 3000 rpm-100% load and 4000 rpm-50% load. This signal has a spectral behaviour similar to

that observed for the scattering at low speed and low load (Figure 5.9). This suggests the presence of an unidentified scattering species in all the engine operating conditions. At high speed conditions the numerical procedure reached an agreement between experimental and theoretical data with an overall mean discrepancy lower than 30%. At 1500 and 2000 rpm, on the other hand, the agreement between experimental and theoretical spectra was poorer and it was not possible to obtain a satisfactory result using BUVESS technique.

5.3.2. ELPI and SMPS measurements.

In order to complete the experimental investigation, Electrical Low Pressure Impactor (ELPI) and Scanning Mobility Particle Sizer (SMPS) were used. The sketch of the experimental setup for the simultaneous measurements with ELPI and SMPS is reported in Figure 5.12.

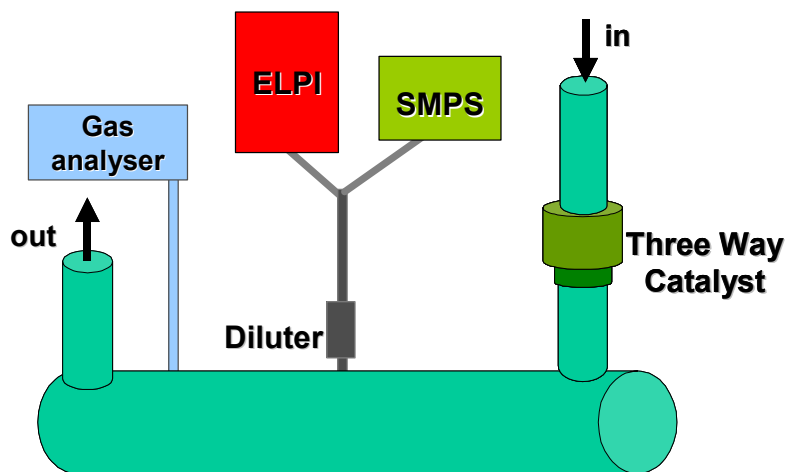


Figure 5.12. Experimental setup for the simultaneous measurements with ELPI and SMPS.

As described in the Chapter 3, ELPI allowed to obtain real time particle size distribution and concentration measurements in the size range 7 nm -10 μm . The ELPI results for all the selected operating conditions are reported in Figure 5.13.

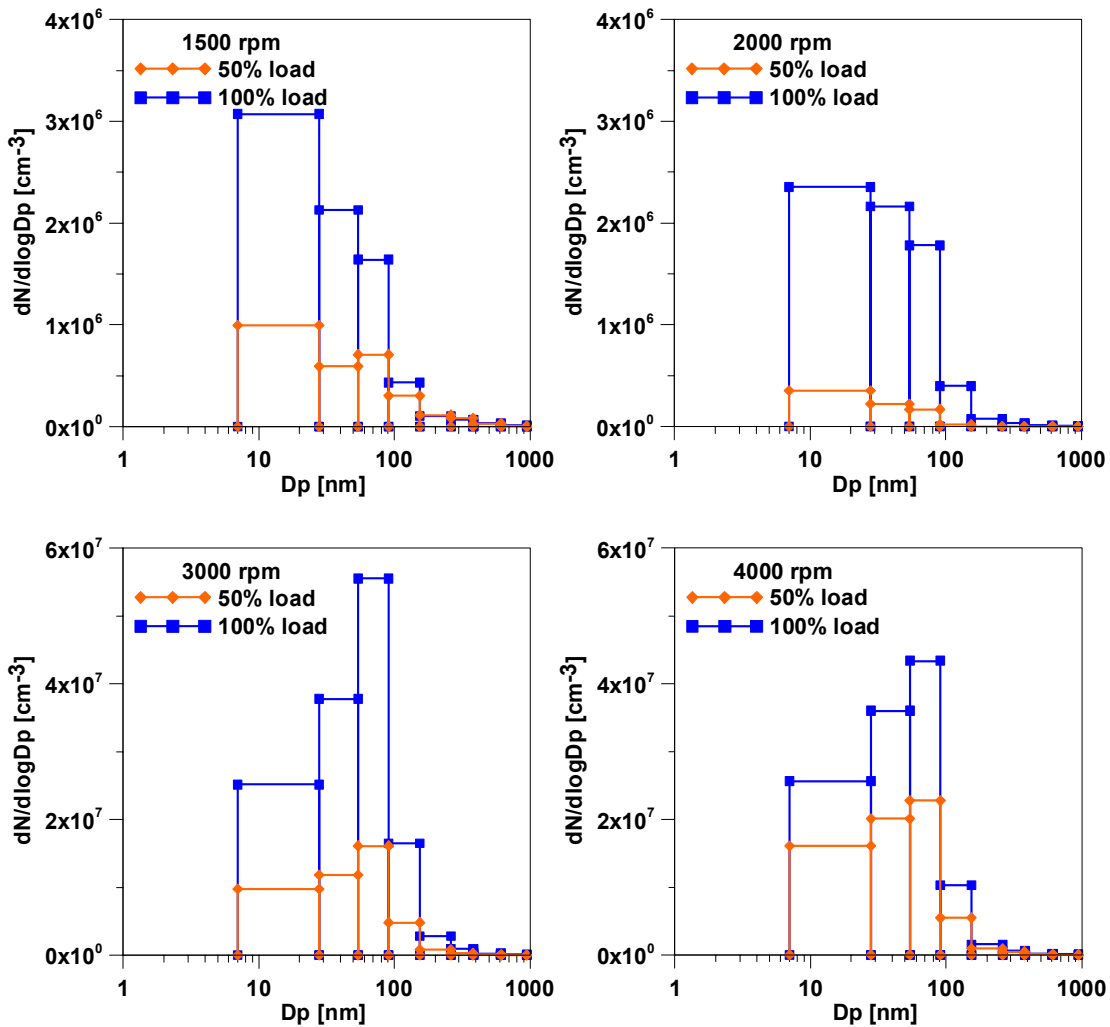


Figure 5.13. Particle number concentration measured by ELPI at the selected operating conditions.

At 1500 and 2000 rpm, the highest particles number concentration was measured at the first ELPI stage that covers the 7 – 28 nm size range. The size distributions show an asymmetrical shape that suggests the presence of maximum for diameters smaller than ELPI lowest size limit. At 3000 and 4000 rpm the size distributions were characterised

by a maximum at the third impactor stage, corresponding to a cut diameter equal to 54 nm. This size distribution reminds of the second mode measured by BUVESS technique due to soot particles. Moreover, it is closed to the typical size distribution of carbonaceous particles detected by ELPI at the exhaust of the common rail diesel engine as reported in Chapter 4.

For all the engine conditions, a little fraction of particles larger than 300 nm was detected and it was always possible to observe an increasing in number concentration at increasing load. According to literature [34] these particle can be produced by lube oil blow-by.

In order to obtain more information about particles smaller than 60 nm, SMPS measurements were carried out [144]. The SMPS operates on the principle of the mobility of a charged particle in an electric field. Particles entering the system are neutralized using a radioactive source. They then go into a Differential Mobility Analyser (DMA) where the aerosol is classified according to electrical mobility, with only particles of a narrow range of mobility exiting through the output slit. In this case a Nano DMA selecting the particles in the range 2–60 nm was used. The monodisperse distribution then goes to a Condensation Particle Counter (CPC), which determines the particle concentration at that size [145].

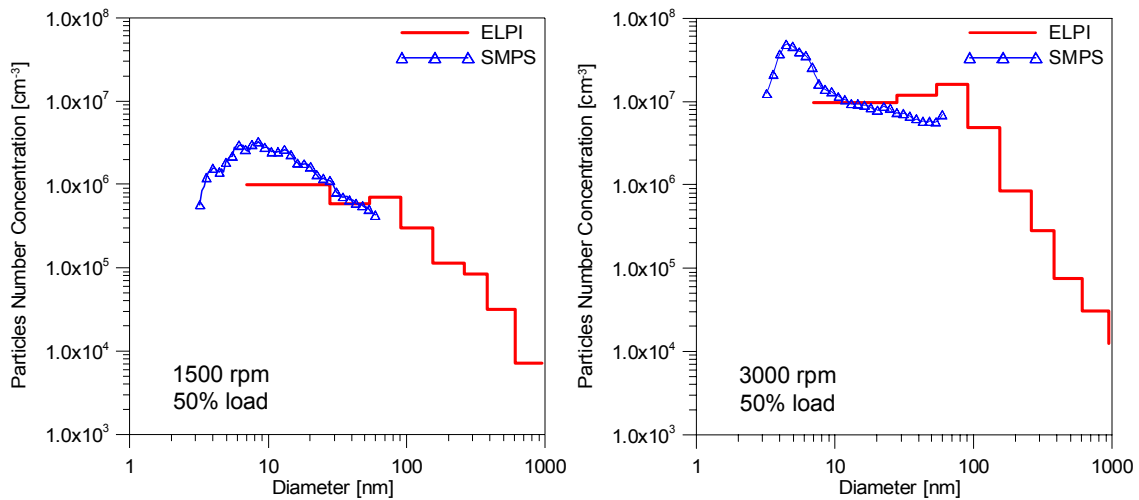


Figure 5.14. Particle number concentration measured by ELPI and SMPS at the selected operating conditions.

A comparison between the results obtained by ELPI and SMPS is shown in figure 5.14. At 1500 rpm - 50% load, a mode of nanoparticles smaller than 10 nm was detected by SMPS; it showed a central diameter around 8 nm and it overlapped with ELPI first stage. A good agreement between ELPI and SMPS size distributions in the overlapping size range was measured at 3000 rpm 50% load, too. Moreover, SMPS detected a size mode below the ELPI detection limit.

Recent experiments carried out by optical methods and AFM (Atomic Force Microscopy) measurements [83] widely applied on flames and on a narrow set of passenger cars, suggest the presence of NOC (Nanoparticles of Organic Carbon) with equivalent diameter around 3 nm. With respect to the vehicles, authors outlined that these nanoparticles were formed in the combustion chamber; then some of them could survive to oxidation in the combustion chamber and in the tree-way catalyst and then they could be emitted at the exhaust. On the other hand, other research results [34] suggest that these particles can be volatile ones resulting from the nucleation of gas phase hydrocarbons during the dilution process.

Thus it is possible to propose that a great number of particle smaller than 15 nm are obtained by the combination of NOC and volatile ones.

It must be observed that the results from different techniques, which are based on different physical/chemical particle properties, are difficult to relate. In particular, the instruments employed in this thesis yield different sizes: mobility diameter for SMPS and aerodynamic diameter for ELPI. Thus, the difference in the measurements between the two systems can be mainly ascribed to the different measuring principle and detection limits.

Conclusions

Optical techniques and commercially available instruments were used at the exhaust of a Common Rail diesel engine and of a Port Fuel Injection Spark Ignition engine to characterise the particles emission in terms of chemical and physical properties with regard to the engines operating conditions.

Two “in situ” optical techniques were applied at the engines undiluted exhaust: Laser Induced Incandescence (LII) and Broadband Ultraviolet-Visible Extinction and Scattering Spectroscopy (BUVESS). LII is able to measure soot primary particles diameter. BUVESS takes advantage of data at several wavelengths to retrieve primary particles size distributions and it gives information about particles chemical nature.

A commercial instrument, Electrical Low Pressure Impactor (ELPI), was used to measure real time particles size distributions in the range 7 nm-10 μm . ELPI evaluates the particles aerodynamic diameters without distinction between primary particles and aggregates.

The diesel engine employed for the experiments was a four-stroke 1910 JTD equipped with a Common Rail injection system, with an Exhaust Gas Recirculation (EGR) cooled system and with a silicon carbide catalysed Diesel Particulate Filter (CDPF). Optical techniques and commercial instruments were applied at the engine exhaust for different operating conditions. In particular, the effects of the EGR and of the aftertreatment device on particles emission were analysed.

EGR allows the reduction of thermal-Nitrogen Oxides but it also influences particles emissions. For this reason, its effect on the balance between the primary particles and the aggregates was evaluated.

By LII, the increasing of the soot primary particles diameters at increasing EGR percentage was revealed for all the engine-operating conditions. This was probably due to the partial oxidation of soot recirculated in the combustion chamber and the successive superficial growth. However, the increasing in primary particles diameter could also be caused by the low oxidation rate of soot at high EGR% due to a reduction of oxygen concentration.

BUVLESS measurements showed the evolution of size distributions and number concentrations of the primary particles. They were constituted by low-graphitic carbon and no change in the chemical nature of particles was observed for all tested conditions even at high EGR%. On the other hand, the EGR had a physical effect on the emitted nanoparticles; in fact it induced the formation of an accumulation mode in the size distribution.

The ELPI measured the particle size distributions with the highest number concentration in the range 54-91 nm showed. At increasing EGR%, the number of accumulation particles increased with respect to the total number, while nucleation particles fraction was reduced. This was due to the agglomeration effect caused by the introduction of particles contained in the exhaust gases into the cylinder.

In conclusion, an increase in primary particles mean size with EGR% is coupled to an increase in aggregates aerodynamic diameter and all the methods also revealed an increase in particles number concentration.

Moreover, with respect to diesel engine exhaust, the effect on the nanoparticles emission of the CDPF filter-loading phase and regeneration were investigated. During the loading phase according to BUVLESS measurements, the particle number concentration was reduced by approximately two orders of magnitude by the filter, but

the shape of the distribution remained approximately the same. Moreover, no change was observed in the nanoparticles chemical nature during the crossing of the CDPF since the catalyst was inactive and the filter had only a physical effect.

Two phases of the regeneration process were recognized. The first one could be considered the fragmentation of the stored particulate; it was characterized by the emission of high number of nanoparticles smaller than 30 nm, low HC concentration and negative numeric filtering efficiency. The second phase consisted in the consumption of the particles stucked on the filter internal surfaces: a reduction of nanoparticles number concentration was revealed for diameters higher than 7 nm. An evolution in terms of size and optical properties of the emitted particles was observed, they showed a carbonaceous nature with different levels of graphitisation depending on the time during the regeneration.

To investigate the nature of particles emitted by gasoline engine, a four-stroke 1242 cc Port Fuel Injection (PFI) Spark Ignition (SI) engine, equipped with a three-way catalyst (TWC) was used.

First, the effect of the TWC on the engine particles emissions at different engine operating conditions was evaluated by means of the ELPI. A reduction in number concentration of 1-2 orders of magnitude when the exhaust gas passed through the TWC was observed for the particles in the first ELPI stage (7 – 28 nm). The primary mechanism for their “removal” probably was the catalytic stripping of volatile hydrocarbon particle precursors. In addition, the number of larger particles was decreased downstream of the catalyst possibly by inertial impaction at the catalyst channel faces. In spite of the number concentration reduction due to the TWC, high number of nanoparticles remained at the engine exhaust. Therefore, the characterisation

of particles emitted by the spark ignition engine was carried out downstream of the TWC for different operating conditions.

LII revealed carbonaceous particles with 30-60 nm mean diameters in the range at high speeds. These particles could be due to the diffusion-controlled flame produced by the ignition of fuel film deposition on the intake valves surface and on the cylinder walls, typical of PFI engines.

In order to investigate a wider range of engine operating conditions and to evaluate the chemical-physical nature of particles also at low engine speeds, BUVESS measurements were performed.

Two particles modes were evaluated by the numerical procedure based on Mie theory for spherical particles: the first one was composed by particles with 30 nm mean diameter and soot optical properties. The second mode was characterised by particles with mean diameter below 10 nm and the optical properties of NOC.

At low speeds, it was not possible to obtain a satisfactory result in terms of size distribution and optical properties using BUVESS technique because the agreement between experimental and theoretical spectra was poor. Thus, further investigation should be carried out for these conditions.

In order to complete the experimental investigation, ELPI and Scanning Mobility Particle Sizer (SMPS) were simultaneously used. At low speed, asymmetrical size distributions with a maximum at the first ELPI stage (7 – 28 nm) suggested the presence of maximum for diameters smaller than ELPI lowest size limit. At high speed the size distributions were characterised by a maximum at the third impactor stage, corresponding to a cut diameter equal to 54 nm. This size distribution reminds of the typical size distribution of carbonaceous particles detected by ELPI at the exhaust of the

common rail diesel engine. For all the engine conditions, a little fraction of particles larger than 300 nm was detected, they could be produced by lube oil blow-by.

A good agreement between ELPI and SMPS size distributions in the overlapping size range was measured for all the conditions even if these instruments yield different sizes: mobility diameter for SMPS and aerodynamic diameter for ELPI. SMPS detected a size mode below the ELPI detection limit. It is possible to propose that a great number of particles smaller than 15 nm are obtained by the combination of Nanoparticles of Organic Carbon (NOC), formed in the combustion chamber and survived to oxidation; and volatile particles, resulting from the nucleation of gas phase hydrocarbons during the dilution process.

In conclusion, the results reported in this thesis show that, in spite of internal combustion engine improvements, further efforts will be necessary to satisfy the particulate number based limits of the upcoming normative. With respect to diesel engines, the introduction of alternative combustion modes, as HCCI, and high efficiency after-treatment devices could be the first positive answers.

About the spark ignition engines, the turbocharged engines can allow the reduction of fuel consumption with respect to an increase of engine performances but make more critical the problem of particles emission, especially in the case of direct injection engines. Thus, a more accurate analysis of the particles formation mechanisms is necessary to better understand the chemical structures of emitted nanoparticles.

Bibliography

[1] Kittelson D.B., *Engines and nanoparticles: a review*, Journal of Aerosol Science 29, 575–588, 1998.

[2] Gaskow B.R., Kittelson, D.B., Ahamadi M.R., Morris J.E., *Exhaust Particulate Emissions from a Direct Injection Spark Ignition Engine*, SAE Paper n. 1999-01-1145, 1999.

[3] Gilmour P.S., Ziesenis A., Morrison E.R., Vickers M.A., Drost E.M., Ford I., Karg E., Mossa C., Schroepel A., Ferron G.A., Heyder J., Greaves M., MacNee W., Donaldson K., *Pulmonary and systemic effects of short-term inhalation exposure to ultrafine carbon black particles*, Toxicol Appl Pharmacol v.15; 195(1): 35-44, 2004.

[4] Oberdorster G., Gelein R.M., Ferin J., Weiss B., *Association of particulate air pollution and acute mortality: involvement of ultrafine particles?*, Inhalation Toxicology v.7: 111–124, 1995.

[5] Donaldson K., Li X.Y., MacNee W., *Ultrafine (nanometer) particle mediated lung injury*, Journal of Aerosol Science 29, 553–560, 1998.

[6] Donaldson K., Stone V., Gilmour P.S., Brown D.M., MacNee W., *Ultrafine particles: mechanisms of lung injury*, Philosophical Transactions of the Royal Society of America 358, 2741–2750, 2000.

[7] Maynard R.L., *New directions: reducing the toxicity of vehicle exhaust*. Atmospheric Environment 34, 2667–2668, 2000.

[8] Nemmar A., Hoet P., Vanquickenborne B., Dinsdale D., Thomeer M., Hoylaerts M.F., Vanbilloen H., Mortelmans L., Nemery B., *Passage of inhaled particles into the blood circulation in humans*, Circulation 105, 411–414, 2002.

[9] <http://www.dieselnet.com>

[10] Merola S.S., Vaglieco B.M., Tornatore C., *Characterization of Nanoparticles Emitted During the Regeneration of Catalyzed Diesel Particulate Filter*, Chemical Engineering Transactions – Volume 10, pp. 507-513 , 2006.

[11] McAughey J.J., Dickens C.J., Rickeard D.J., Bateman J.R., Kwon Y.K., *Exhaust Particulate Size Distribution: Vehicle and Fuel Influences in light Duty Vehicles*, SAE Paper n. 961980, 1996.

[12] Hall D.E., Goodfellow C.L., Heinze P., *A study of the Size, number and Mass Distribution of the Automotive Particulate Emission from European light Duty Vehicles*, SAE Paper n. 982600, 1998.

[13] Rubino L., Crane R.I., Shrimpton J.S., Arcoumanis C., *An electrostatic trap for control of ultrafine particle emissions from gasoline-engined vehicles*, Proceedings of the I MECH E Part D Journal of Automobile Engineering Vol. 219 Page: 535 – 546, 2005.

[14] Kayes D. and Hochgreb S., *Investigation of the Dilution Process for measurements of particulate Matter from spark Ignition Engines*, SAE paper number 982601, 1998.

[15] Gaskow B.R., Kittelson D.B., Abdul-khalek I.S., Ahamadi M.R., Morris J.E., *Characterization of Exhaust Particulate Emissions from a Spark Ignition Engine*, SAE paper number 980528, 1998.

[16] Cadle S.H., Mulawa P., Hunsanger E.C., Nelson K., Ragazzi R.A., Barrett R., Gallagher G.L., Lawson D.R., Knapp K.T., Snow R., *Measurement of Exhaust Particulate Matter Emissions from In-Use Light-Duty Motor Vehicles in the Denver, Colorado Area, Coordinating Research Council Project E-24-1 Final Report*, CRC, Atlanta, GA, 142 pp., 1998.

[17] Abdul-Khalek I.S., Kittelson, D.B., Brear F., *The influence of dilution conditions on diesel exhaust particle size distributions measurements*, SAE Paper n. 1999-01-1142, 1999.

[18] Witze P.O., *Diagnostics for the Measurement of Particulate Matter Emissions from Reciprocating Engines*, The Fifth International Symposium on Diagnostics and Modeling of Combustion in Internal Combustion Engines, Nagoya, Japan, July 1–4, 2001.

[19] Hunt A.J., Quinby-Hunt M.S., Shepherd I.G., *Diesel Exhaust Particle Characterization by Polarized Light Scattering*, SAE Paper n. 982629, 1998.

[20] Merola, S.S., Vaglieco, B.M., Di Iorio, S., *Nanoparticles at Internal Combustion Engines Exhaust: Effect on Urban Area*, SAE Paper n. 2006-01-3006, 2006.

[21] Di Iorio S., Merola S.S., Vaglieco B.M., Tornatore C., *Diesel Exhaust Nanoparticles Characterization by Multiwavelength Techniques*, Laser Induced Incandescence and ELPI, SAE Paper n. 2005-24-021, 2005.

[22] Corcione F.E., Consales S., Formisano G., Merola S.S., Vaglieco B.M., *Determination of Size of Fuel Droplets and Soot Particles in a Diesel Engine by Broadband Extinction and Scattering Spectroscopy*, Part & part System. Characterization vol.18 n°5-6 pag. 235-242, 2001.

[23] Vaglieco B.M., Monda O., Corcione F.E., Menguc M.P., *Optical and Radiative Properties of Particulates at Diesel Engine Exhaust*, Combust. Sci. and Tech. v.102: 283-299, 1994.

[24] Seinfeld J.H., *Atmospheric chemistry and physics of air pollution*, ed. John Wiley & Sons, New York, 1986.

[25] <http://www.epa.gov/eogap1/module6/matter/character/character.htm#charapar>

[26] Chalupa D.C., Morrow P.E., Oberdörster G., Utell M. J., Frampton M.W., *Ultrafine particle deposition in subjects with asthma.*, Environ Health Perspect. 2004 June; 112(8): 879–882, 2004.

[27] Health Effects Institute - Research Report 126 - December 2004.

[28] Abu-Allaban M., Gillies J.A., Gertler A.W., Clayton R., Proffitt D., *Motor Vehicle Contributions to Ambient PM10 and PM2.5 at Selected Urban Areas in the USA*, Journal Environmental Monitoring and Assessment, Publisher Springer Netherlands, Vol., N. 1-3 / September, 2007.

[29] Giovannini F. and Grechi D., *Stima delle variazioni di emissione di particolato in area urbana conseguenti all'applicazione di restrizioni alla circolazione di alcune tipologie di veicoli*, Rapporto per Organo Tecnico, ed. ARPAT - Dipartimento di Firenze (Italia), 2003.

[30] Kittelson D.B., Johnson J., Watts W., Wei Q., Drayton M., Paulsen D. Bukowicki N., *Diesel Aerosol Sampling in the Atmosphere*, Society of Automotive Engineers Technical Paper 2000-01-2212: 1–8, 2000.

[31] Kittelson D., Johnson D., Watts W., *Diesel Aerosol Sampling Methodology*, CRC E-43 annual report available at <http://www.crcao.com>, 2002.

[32] Burtscher H., *Particulate Emissions from Diesel Engines: a Review*, Journal of Aerosol Science 36 896–932, 2005.

[33] Storey J.M.E., Slider S., Blom D.A., Higinbotham E., *Particulate Emissions from a Pre-Emissions Control Era Spark-Ignition Vehicle: A Historical Benchmark*, SAE Paper n. 2000-01-2213, 2000.

[34] Graskow B.R., Kittelson D.B., Ahamadi M.R. Morris J.E., *Exhaust Particulate Emissions from Two Port Fuel Injected Spark Ignition Engines*, SAE Paper n. 1999-01-1144, 1999.

[35] Di Iorio S., Merola S.S., Vaglieco B.M., Tornatore C., *Nanoparticles Characterization at Spark Ignition Engine Exhaust*, SAE Paper n. 2005-24-010, 2005.

[36] Hall D.E., *A Study of the Number, Size & Mass of Exhaust Particles Emitted from European Diesel and Gasoline Vehicles under Steady State and European Driving Cycle Conditions*, Report n° 98/51, CONCAWE, Brussels 1998.

[37] Pattas K., Kyriakas N., Samaras Z., Pistikopoulos P., Ntziachristos L., *Effect of DPF on Particulate Size Distribution Using an Electrical Low Pressure Impactor*, SAE Paper n. 980544, 1998.

[38] *Chemical Methods for the Measurement of Non-Regulated Diesel Emissions*. 1993 SAE Handbook, Vol.3, Engines, Fuels Lubricants, Emissions and Noise, Society of Automotive Engineers 1993.

[39] Kittelson D.B., Watts W.F., Johnson J.P., *Ultrafine and Nanoparticle Emissions: A New Challenge for Internal Combustion Engine Designers*, Intern. Conf. "Engines of Sustainable Development", Naples, 2003.

[40] Jung H., Kittelson D.B., Zachariah M.R., *The influence of engine lubricating oil on diesel nanoparticle emissions and kinetics of oxidation*, SAE Paper n. 2003-01-3179, 2003.

[41] <http://www.nett.ca/faq/diesel-1.html>

[42] Kittelson D.B., *Recent Measurements of Nanoparticle Emissions from Engines*, Proceedings of the meeting on Current Research on Diesel Exhaust Particles Japan Association of Aerosol Science and Technology, TOKYO, JAPAN, 9 January 2001

[43] Zhao F., Harrington D.L., Lai M-C.D., *Automotive Gasoline Direct-Injection Engines*, Warrendale, PA: SAE, 2002.

-
- [44] Andrews G.E. and Ahamed F.M., *The Composition of Spark Ignition Engine Steady State Particulate Emissions*, SAE Paper n. 1999-01-1143, 1999.
- [45] Haynes B.S. and Wagner H.Gg., *Soot formation*, Prog. Energy Combust. Sci. 7, 229–273, 1981.
- [46] Kubo S., *In-cylinder Soot Formation Mechanism - TOYOTA CENTRAL R&D LABS., INC*, 2006.
- [47] Wang H. and Frenklach M., *Transport properties of polycyclic aromatic hydrocarbons for flame modeling*, Combust. Flame. 96, 163–170, 1994.
- [48] Griesheimer J. and Homann K.-H., *Large molecules, radicals, ions, and small soot particles in fuel-rich hydrocarbon flames. Part II: aromatic radicals and intermediate PAHs in a premixed low-pressure naphthalene/oxygen/argon flame*, Proc. Comb. Inst. 27, 1753–1759, 1998.
- [49] Ahrens J., Keller A., Kovacs R., Homann K.-H., *Large molecules, radicals, ions, and small soot particles in fuel-rich hydrocarbon flames. Part III: REMPI Mass spectrometry of large flame PAHs and Fullerenes and their quantitative calibration through sublimation.*, Ber. Bunsenges. Phys. Chem. 102(12), 1823–1839, 1998.
- [50] Böhm H. and Jander H., *PAH formation in acetylene-benzene pyrolysis*, Phys. Chem. Chem. Phys. 1, 3775–3781, 1999.
- [51] Violi A., D’Anna A., D’Alessio A., Sarofim A.F., *Modeling Aerosol Formation in Opposed-Flow Diffusion Flames*, Chemosphere 51(10), 1047-1054, 2003.
- [52] Violi A., D’Anna A., D’Alessio A., *A kinetic model of particulate carbon formation in rich premixed flames of ethylene and benzene*, Clean Air-International Journal on Energy for a Clean Environment 5(3), 1-18, 2004.

[53] Richter H., Granata S., Green W.H., Howard J.B., *Detailed modeling of PAH and soot formation in a laminar premixed benzene/oxygen/argon low-pressure flame*, Proc. Comb. Inst. 30, 1397–1405, 2005.

[54] Agafonov G.L., Naydenova I., Vlasov P.A., Warnatz J., *Detailed kinetic modeling of soot formation in shock tube pyrolysis and oxidation of toluene and n-heptane*, Proc. Comb. Inst. 31, 575–583, 2007.

[55] Frenklach M. and Wang H., *Detailed modeling of soot particle nucleation and growth*, Proc. Comb. Inst. 23, 1559–1566, 1991.

[56] Frenklach M. and Wang H., *Detailed kinetic modeling of soot particle formation*, Springer 59, 1994.

[57] Neoh K.G., Howard J.B., Sarofim A.F., *Particulate Carbon Formation During Combustion*, 261. Plenum Press, New York, 1981.

[58] Pfefferle L.D., Bermudes G., Byle J., *Soot formation in combustion., Kapitel Benzene and higher hydrocarbon formation during alene pyrolysis*. Springer-Verlag, Berlin/Heidelberg, 1994.

[59] Frenklach M. and Ebert L.B., *Comment on the proposed role of spheroidal carbon clusters in soot formation*, J. Phys. Chem. 92, 561–563, 1988.

[60] Miller J.H., *The kinetics of polynuclear aromatic hydrocarbon agglomeration in flames*. Proc. Comb. Inst. 23, 91 1990.

[61] D'Anna A., D'Alessio A., Minutolo P., *Soot Formation in Combustion, Mechanisms and models*, 83. Springer-Verlag, Heidelberg, 1994.

[62] Warnatz J., Maas U., Dibble R.W., *Physical and chemical fundamentals, modeling and simulation, experiments, pollutant formation*, 4rd Edition. Springer-Verlag Berlin, Heidelberg, 2006.

[63] Lee K.O. and Zhu J., *Evolution in Size and Morphology of Diesel Particulates Along the Exhaust System*, SAE Paper n. 2004-01-1981, 2004.

[64] DeCarlo P., Worsnop D.R., Slowik J.G., Davidovits P., Jimenez J.L., *Particle Morphology and Density Characterization by Combined Mobility and Aerodynamic Diameter Measurements. Part I: Theory*, *Aerosol Sci. Technol.* 38(12):1185-1205, 2004.

[65] Baron P.A. and Willeke K., *Gas and Particle Motion. In Aerosol Measurement: Principles, Techniques, and Applications*, edited by P. A. Baron and K. Willeke. Wiley, New York, pp. 61–97, 2001.

[66] Hinds W.C., *Aerosol Technology: Properties, Behavior, and Measurement of Airborne Particles.*, Wiley, New York, 1999.

[67] Flagan R.C., *Electrical Techniques, in Aerosol Measurement: Principles, Techniques, and Applications*, edited by P. A. Baron and K. Willeke, John Wiley, New York, pp. 537–568, 2001.

[68] Chakrabarti B., Singh M., Sioutas C., *Development of a Near Continuous Monitor for Measurement of the Sub-150 nm PM Mass Concentration*, *Aerosol Sci. Technol.* 38(S1):239–252, 2004.

[69] Zhang Q., Canagaratna M.R., Jayne J.T., Worsnop D.R., Jimenez J.L., *Time and Size-Resolved Chemical Composition of Submicron Particles in Pittsburgh-Implications for Aerosol Sources and Processes*, *J. Geophys. Res.-Atmos.*, 2004.

[70] Baron P.A., Sorensen C.M., Brockmann J.E., *Nonspherical Particle Measurements: Shape Factors, Fractals, and Fibers*, In *Aerosol Measurement: Principles, Techniques, and Applications*, edited by P. A. Baron and K. Willeke. John Wiley, New York, pp. 705–749, 2001.

-
- [71] Park K., Kittelson D.B., McMurry P.H., *Structural Properties of Diesel Exhaust Particles Measured by Transmission Electron Microscopy (TEM): Relationships to Particle Mass and Mobility*, *Aerosol Sci. Technol.* 38(9):881–889, 2004.
- [72] Park K., Cao F., Kittelson D.B., McMurry P.H., *Relationship Between Particle Mass and Mobility for Diesel Exhaust Particles*, *Environ. Sci. Technol.* 37(3):577–583, 2003.
- [73] Schmidt-Ott A., Baltensperger U., Gaggeler H.W., Jost D.T., *Scaling Behavior of Physical Parameters Describing Agglomerates*, *J. Aerosol Sci.* 21(6):711–717, 1990.
- [74] Bohren C.F. and Huffman D.R., *Absorption and Scattering of Light by Small Particles*, Wiley-Interscience, New York, 1983.
- [75] Merola S.S., Vaglieco B.M., Zarinchang J., *Simultaneous Detection of NO_x and Particulate in Exhaust of a CR Diesel Engine by UV-Visible Spectroscopy*, SAE Paper n. 2003-01-0786, vol.112 SAE transaction Journal Engines pp. 1207-1215, 2003.
- [76] Kirkevåg A., Iversen T., Dahlback A., *On radiative effect of black carbon and sulphate aerosols*, *Atmospheric Environment*, 33, 2621-2635, 1999.
- [77] Manzello S.L., Lenhart D.B., Yozgatligil A., Donovan M.T., Mulholland G.W., Zachariah M.R., Tsang W., *Soot particle size distributions in a well-stirred reactor/plug flow reactor*, *Proceedings of the Combustion Institute* 31 (2007) 675–683, 2007.
- [78] Rose D., Wehner B., Ketzler M., Engler C., Voigtländer J., Tuch T., Wiedensohler A., *Atmospheric number size distributions of soot particles and estimation of emission factors*, *Atmos. Chem. Phys.*, 6, 1021–1031, 2006.
- [79] Taft A. and Philip H.R., *Phys. Rev.* 138:A197, 1965
- [80] Di Nardo R.P. and Goland A.N., *J. Opt. Soc. Am.* 61, 1321, 1964.

[81] Maier-Komor P., *A Rapid and Accurate Method for Measuring the Thickness of Extremely thin Targets*, Proceedings of the fifth Conference of the International Nuclear Target Development Society - October, 1976.

[82] Chang H. and Charalampopoulos T.T., *Determination of the wavelength dependence of refractive indices of flame soot*, Proc. Royal Soc. London A, 430, 577-591, 1990.

[83] D'Alessio A., D'Anna A., Barone A.C., Borghese A., Speranza L., Minutolo P., *Combustion-Generated Nanoparticles of Organic Carbon in Flames and Engine Exhausts*, SAE Paper n. 2005-24-011, 2005.

[84] Levoni C., Cervino M., Rodolfo G., Torricella, F., *Atmospheric Aerosol Optical Properties: a Database of Radiative Characteristic for Different Components and Classes*, Applied Optics, Vol. 36, No. 30, pp. 8031 – 8041, 1997.

[85] Merola S.S. and Vaglieco B.M., *Spectroscopic Characterisation of Nanoparticle Modes at the Exhaust of a CR Diesel Engine Equipped with Particulate Filter*, SAE Paper n. 2003-01-54, 2003.

[86] Ackerman T.P. and Toon O.B., *Absorption of visible radiation in atmosphere containing mixtures of absorbing and nonabsorbing particles*, Applied Optics, v.20 n.20, 3661-3668, 1981.

[87] Egan W.G. and Hilgeman T., *Anomalous refractive index of submicron sized particulates*, Applied Optics, v.19 n.22, 3724-3727, 1980.

[88] Kihong P., Kittelson D.B., Zachariah M.R., McMurry P.H., *Measurement of inherent material density of nanoparticle agglomerates*, Journal of Nanoparticle Research 6: 267–272, 2004.

[89] Melton L.A., *Soot Diagnostics Based on Laser Heating*, Appl. Opt. v. 23: 2201-2208, 1984.

[90] Schraml S., Will S., Leipertz A., *Simultaneous Measurement of Soot Mass Concentration and Primary Particle Size in the Exhaust of a DI Diesel Engine by Time-Resolved Laser-Induced Incandescence (TIRE-LII)*, SAE Paper n. 1999-01-0146, 1999.

[91] De Iuliis S., Cignoli F., Benecchi S., Zizak G., *Determination of soot parameters by a two-angle scattering-extinction technique in an ethylene diffusion flame*, Applied Optics v.37: 7865-7874, 1998.

[92] Green R.M. and Witze P.O., *Laser-induced incandescence and elastic-scattering measurements of particulate-matter volume fraction changes during passage through a dilution tunnel*, Proceedings of the 10th International Symposium on Applications of Laser Techniques to Fluid Mechanics, Lisbon, July, 2000.

[93] McCoy B.J. and Cha C.Y., *Transport Phenomena in the Rarefied Gas Transition Regime*, Chemical Engineering Science 29: 381-388, 1974.

[94] Snelling D.R., Smallwood G.J., Gülder Ö.L., Bachalo W.D., Sankar S., *Soot Volume Fraction Characterization Using the Laser-Induced Incandescence Detection Method*, Proceedings of the 10th International Symposium on Applications of Laser Techniques to Fluid Mechanics, Lisbon, Portugal, July, 2000.

[95] Bachalo W.D., Sankar S.V., Smallwood G.J. Snelling D.R., *Development of the Laser-Induced Incandescence Method for the Reliable Characterization of Particulate Emissions*, 11th International Symposium on Application of Laser Techniques to Fluid Mechanics, Lisbon, Portugal, July, 2002.

[96] Merola S.S., Vaglieco B.M., Di Iorio S., *Nanoparticles at Internal Combustion Engines Exhaust: Effect on Urban Area*, SAE Paper n. 2006-01-3006, 2006.

[97] Maricq M., Podsiadlik D., Chase R., *Size Distributions of Motor Vehicle Exhaust PM: A Comparison Between ELPI and SMPS Measurements*, Aerosol Science and Technology 33: pp. 239-260, 2000.

-
- [98] Virtanen A., Ristimäki J., Marjamäki M., Vaaraslahti K., Keskinen J., *Effective density of Diesel Exhaust Particles as a Function of Size*, SAE Paper n. 2002-01-0056, 2002.
- [99] Witze P.O., Chase R.E., Maricq M.M., Podsiadlik D.H., Xu N., *Time-Resolved Measurements of Exhaust PM for FTP-75: Comparison of LII, ELPI, and TEOM Techniques*, SAE Paper n. 2004-01-0964, 2004.
- [100] Maricq M., Xu N., Chase R.E., *Measuring Particulate Mass Emissions with the Electrical Low Pressure Impactor*, *Aerosol Science & Technology*. Vol 40, pp. 68 – 79, 2006.
- [101] Van Gulijk C., Marijnissen J.C.M., Makkee M., Moulijn J.A., *Restriction for the ELPI in Diesel Particulate Measurements*, *J. Aerosol Sci.* 32:1117–1130, 2001.
- [102] Van Gulijk C., Marijnissen J.C.M., Makkee M., Moulijn J.A., *The Choice of Instrument (ELPI and/or SMPS) for Diesel Soot Particulate Measurements*, SAE Paper n. 2003-01-0784, 2003.
- [103] Van Gulijk C., Marijnissen J.C.M., Makkee M., Moulijn J.A., Schmidt-Ott A., *Measuring Diesel Soot with a Scanning Mobility Particle Sizer and an Electrical Low-Pressure Impactor: Performance Assessment with a Model for Fractal Like Agglomerates*, *J. Aerosol Sci.* 35:633–655, 2004.
- [104] Zervas E., Dorlhène P., Forti L., Perrin C., Momique J.C., Monier R., Ing H., Lopez B., *Interlaboratory Test of Exhaust PM Using ELPI*, *Aerosol Science and Technology*, 39:4, 333 – 346, 2005.
- [105] Canale S. and Scotton R., *Calcolo della percentuale di EGR – Motori – Sistemi Diesel ed Emissioni*, Orbassano, January, 1992.
- [106] Heywood J.B., *Internal Combustion Engine Fundamentals*, McGraw-Hill, 1988.

-
- [107] Mörsch O. and Sorsche P., *Investigation of Alternative Methods to Determine Particulate Mass Emissions*, UNECE/WP.29/GRPE report 2001.
- [108] Zhao H., Ladommatos N., *Engine combustion instrumentation an diagnostics*, SAE International, 2001.
- [109] Borghese A. and Merola S.S., *Time Resolved Spectral and Spatial Description of Laser-Induced Breakdown in Air as a Pulsed, Bright and Broadband Ultraviolet-Visible Light Source*, *Applied Optics*, 37: 3977-3083, 1998.
- [110] Snelling D. R., Smallwood G.J., Sawchuk R.A., Neil W.S., Gareau D., Chippior W.L., Liu F., Gülder Ö.L., Bachalo W.D., *Particulate Matter Measurements in a Diesel Engine Exhaust by Laser-Induced Incandescence and Standard Gravimetric Procedure*, SAE Paper n. 1999-01-3653, 1999.
- [111] Schulz C., Kock B.F., Hofmann M., Michelsen H., Will S., Bougie B., Suntz R., Smallwood G., *Laser-induced incandescence: recent trends and current questions*. *Applied Physics B: Lasers and Optics*. 83(3):333-354, 2006.
- [112] Acquaviva S. and De Giorgi M.L., *High-resolution investigations of C₂ and CN optical emissions in laser-induced plasmas during graphite ablation*, *J. Phys. B: At. Mol. Opt. Phys.* 35 795-806, 2002.
- [113] Bengtsson P.-E. and Aldén M., *Soot-visualization strategies using laser techniques*, *Appl. Phys. B* 60, 51-59, 1995.
- [114] Vander Wal R.L., *Development and Characterization of Laser-Induced Incandescence Towards Nanoparticle (Soot) Detection*, NASA/CR-2000-2093, 09, 2000.
- [115] Maricq M., *Measuring motor vehicle PM emissions: Current issues and future directions*, Lexington meeting December 11, 2002.

[116] Lundquist U., Smedler G., Stalhammar P., *A comparison between different EGR systems for HD diesel engines and their effects on performance, fuel consumption and emissions.*, SAE Paper n. 2000-01-0226, 2000.

[117] Ladommatos N., Abdelhalim S., Zhao H., *The Effects of Exhaust Gas Recirculation on Diesel Combustion and Emissions*, International Journal of Engine Research, v.1-n.1, pp.107-126, 28 February, 2000.

[118] Agrawal A.K., Singh S.K., Sinha S., Shukla M.K., *Effect of EGR on the exhaust gas temperature and exhaust opacity in compression ignition engines*, Sādhanā, v.29, Part 3, June 2004, pp.275–284, 2004.

[119] Sluder C.S., Wagner R.M., Storey J.M.E., Lewis S.A., *Implications of Particulate and Precursor Compounds Formed During High-Efficiency Clean Combustion in a Diesel Engine*, SAE Paper n. 2005-01-3844, 2005.

[120] Kihong P., Kittelson D., McMurry P., *Structural Properties of Diesel Exhaust Particles Measured by Transmission Electron Microscopy (TEM): Relationships to Particle Mass and Mobility*, Aerosol Science and Technology, v.38-n.9, pp. 881-889(9), 2004.

[121] Nagle J. and Strickland-Constable R.F., *Fifth Carbon Conference*, v.1, p.154, Pergamon, Oxford, 1962.

[122] Merola S.S., Tornatore C., Vaglieco B.M., *Effect of EGR on nanoparticles at Common-rail diesel engines exhaust*, PTNSS Silniki Spalinowe/Combustion Engines - Nr 2007-SC3- 075 pp. 206-217, 2007.

[123] Di Iorio S., Merola S.S., Tornatore C., Vaglieco B.M., *Effect of Forced EGR on Chemical and Physical Nature of Particles at Diesel Engine Exhaust*, Proceedings of the 6th Symposium Towards Clean Diesel Engines - - Congress Centre, Continental Terme Hotel Ischia (Naples) – Italy-June 20th – 22nd, 2007.

[124] Pace L., Konieczny R., Presti M., *Metal Supported Particulate Matter-Cat, A Low Impact and Cost Effective Solution for a 1.3 Euro IV Diesel Engine*, SAE Paper n. 2005-01-0471, 2005.

[125] Bockhorn H. (Editor), *Soot Formation in Combustion-Mechanisms and Models*, volume 59 of Springer Series in Chemical Physics, Springer-Verlag, 1994.

[126] Seinfeld J.H. and Pandis S.P., *Atmospheric chemistry and physics*, John Wiley, Sons, Inc., New York, 1998.

[127] Auckenthaler T.S., Onder C.H., Geering H.P., *Online Estimation of the Oxygen Storage Level of a Three-Way Catalyst*, SAE Paper n. 2004-01-0525, 2004.

[128] Black J., Eastwood P.G., Tufail K., Winstanley T., Hardalupas Y., Taylor A.M.K.P., *Inter-Correlations Between Smoke Opacity, Legal Particulate Sampling (LPS) and TEOM, During Transient Operation of a Diesel Engine*, SAE Paper n. 2007-01-2060, 2007.

[129] Lapuerta M., Martos F.J., Cárdenas M.D., *Determination of light extinction efficiency of diesel soot from smoke opacity measurements*, Meas. Sci. Technol. 16 2048–2055, 2005.

[130] Merola S.S., Gambi G., Allouis C., Beretta F., Borghese A., D'Alessio A., *Analysis of exhausts emitted by i.c. engines and fluorescence spectroscopy*, Chemosphere 42 827–34, 2001.

[131] AVL 2001 Smoke Measurement AVL LIST GMBH, Graz.

[132] Prati M.V., Rapone M., Della Ragione L., Meccariello G., Iaccio I., Costagliola M.A., *An experience with an on-board opacity measurement campaign on buses running in Italian cities and engine test bed correlation of PM emissions.*, Abstracts of International Conference on Transport and Environment: A Global Challenge. Technological and Policy Solutions, Milano (Italy), p. 68, 2007.

[133] Abdul-Khalek I.S. and Kittelson D.B., *Real Time Measurement of Volatile and Solid Exhaust Particles Using a Catalytic Stripper*, SAE Paper n. 950236, 1995.

[134] Merola S.S. and Vaglieco B.M., *Optical Investigations of Valve Firing in PFI Spark-Ignition Engine*, Proc. ECOS 2007 Conference, Paper n° ECOS07-M01 – Volume I, page 105, 2007.

[135] Maricq M.M., Podsiadlik D.H., Chase R.E., *Gasoline Vehicle Particle Size Distributions: Comparison of Steady State, FTP, and US06 Measurements*, Environ. Sci. Technol. 1999, 33, 2007-2015, 1999.

[136] Merola S.S., Sementa P., Tornatore C., Vaglieco B.M., *Effect of fuel film deposition on Combustion Process in PFI SI engine.*, JOURNAL OF KONES Powertrain and Transport – Vol. 14, Nr. 3, pp. 395-402, 2007.

[137] Costanzo V.S. and Heywood J.B., *Mixture Preparation Mechanisms in a Port Fuel Injected Engine*, SAE paper n. 2005-01-2080, 2005.

[138] Gold M.R., Arcoumanis C., Whitelaw J.H., Gaade J., Wallace S., *Mixture Preparation Strategies in an Optical Four-Valve Port-Injected Gasoline Engine*, Int. J. of Engine Research, Vol. 1, N. 1, 41-56, 2000.

[139] Meyer R. and Heywood J.B., *Liquid Fuel Transport Mechanisms into the Cylinder of a Firing Port-Injected SI Engine During Start Up*, SAE Paper n. 970865, 1997.

[140] Shin Y., Cheng W.K., Heywood J.B., *Liquid Gasoline Behaviour in the Engine Cylinder of a SI Engine*, SAE Paper n. 941872, 1994.

[141] Zhu G.S., Reitz R.D., Xin J., Takabayashi T., *Modelling Characteristics of Gasoline Wall Films in the Intake Port of Port Fuel Injection Engines*, Int. J. of Engine Research, Vol. 2, N. 4, 231-248, 2001.

[142] Drake M.C., Fansler T.D., Solomon A.S., Szekely G.A. Jr., *Piston fuel films as a source of smoke and hydrocarbon emissions from a wall-controlled spark-ignited direct-injection engine*, SAE Paper n. 2003-01-0547, 2003.

[143] Karcher W., *Spectral Atlas of Polycyclic Aromatic Compounds*, Vol. 1 Karcher, W et al. ed., Kluwer Academic Publ, 1988.

[144] Di Iorio S., Merola S.S., Vaglieco B.M., D'Anna A., Bichi E., Minutolo P., *Emissions of Ultrafine Particles from a Port Fuel Injection Spark Ignition Engine*, Proceedings of the 10th International Congress on Combustion By-Products and their Health Effects, p 199, Ischia (Naples), June 17-20, 2007.

[145] <http://cloudbase.phy.umist.ac.uk/field/instruments/smps.htm>

This is a fact. And a fact is the most stubborn thing in the world.

Michail Bulgakov

Ringraziamenti

Grazie a Simona Merola per aver messo a mia disposizione tutte le conoscenze e la passione che possiede e per il suo affetto, di cui non potrei fare a meno. Le sono grata per avermi sostenuta nei momenti in cui credevo di non farcela perché, come diciamo io e lei, il mondo è come una grande uscita della tangenziale a Fuorigrotta: “homo homini lupus”;

grazie a Bianca Vaglieco, perché è merito suo se l’Istituto Motori può vantare un gruppo così affiatato e così competente: io sono stata fortunata a trovarlo;

grazie ai professori D’Anna e D’Alessio per il loro appoggio e per i loro suggerimenti.

Grazie agli altri elementi del gruppo di ricerca di cui faccio parte ed associati:

Ezio Mancaruso, Silvana Di Iorio, Bruno Sgammato, Gianni Cantilena. Un grazie speciale va a Carlo Rossi, esperto tecnico motorista specializzato e persona che crede con tutte le sue forze in quello che fa senza risparmiarsi mai nel lavoro. Grazie a Paolo Sementa per aver deciso di essere mio amico e per la sua visione ottimistica della vita ed a Paolo Saccomanno che nella fase finale del dottorato mi ha dato una mano con buona musica e preziosi consigli.

Grazie alla mia famiglia: a mia madre Marisa ed a mio padre Salvatore perché è stata la loro presenza a darmi sicurezza e forza, il loro amore a fare di me quello che sono oggi e la loro intelligenza a rendermi capace di affrontare i momenti difficili; a mio fratello Giovanni che nonostante le diversità di pensiero e di stile crede in me e mi rende fiera di ciò.

Grazie agli amici che mi hanno accompagnato: Vincenzo, conosciuto per merito del lavoro e conservato gelosamente; Gaia, sempre presente dopo anni (e non è facile con me); il gruppo di capoeira Triarte e Francesco.

Grazie a Luciano per le serate ad aspettarmi fuori l’Istituto Motori, per le parole ed i silenzi di comprensione, per essere capace di ridimensionare i miei timori con poche parole e per il suo amore.

“Siamo quello che lasciamo negli altri” e ci portiamo dentro, passo dopo passo, quello che gli altri lasciano in noi.

Cinzia